



Publication Year	2020
Acceptance in OA@INAF	2023-10-04T12:17:38Z
Title	High-resolution, 3D radiative transfer modelling. V. A detailed model of the M 51 interacting pair
Authors	Nersesian, Angelos; Viaene, Sébastien; De Looze, Ilse; Baes, Maarten; Xilouris, Emmanuel M.; et al.
DOI	10.1051/0004-6361/202038939
Handle	http://hdl.handle.net/20.500.12386/34425
Journal	ASTRONOMY & ASTROPHYSICS
Number	643

High-resolution, 3D radiative transfer modelling

V. A detailed model of the M 51 interacting pair

Angelos Nersesian¹, Sébastien Viaene², Ilse De Looze^{2,3}, Maarten Baes², Emmanuel M. Xilouris¹,
Matthew W. L. Smith⁴, Simone Bianchi⁵, Viviana Casasola⁶, Letizia P. Cassarà⁷, Christopher J. R. Clark⁸,
Wouter Dobbels², Jacopo Fritz⁹, Frédéric Galliano¹⁰, Suzanne C. Madden¹⁰,
Aleksandr V. Mosenkov^{11,12}, and Ana Trčka²

¹ National Observatory of Athens, Institute for Astronomy, Astrophysics, Space Applications and Remote Sensing, Ioannou Metaxa and Vasileos Pavlou, 15236 Athens, Greece
e-mail: a.nersesian@noa.gr

² Sterrenkundig Observatorium Universiteit Gent, Krijgslaan 281 S9, 9000 Gent, Belgium

³ Department of Physics and Astronomy, University College London, Gower Street, London WC1E 6BT, UK

⁴ School of Physics and Astronomy, Cardiff University, The Parade, Cardiff CF24 3AA, UK

⁵ INAF – Osservatorio Astrofisico di Arcetri, Largo E. Fermi 5, 50125 Florence, Italy

⁶ INAF – Istituto di Radioastronomia, Via P. Gobetti 101, 4019 Bologna, Italy

⁷ INAF – Istituto di Astrofisica Spaziale e Fisica Cosmica, Via Alfonso Corti 12, 20133 Milan, Italy

⁸ Space Telescope Science Institute, 3700 San Martin Drive, Baltimore, Maryland 21218, USA

⁹ Instituto de Radioastronomía y Astrofísica, UNAM, Campus Morelia, AP 3-72, 58089 Michoacán, Mexico

¹⁰ Laboratoire AIM, CEA/DSM – CNRS – Université Paris Diderot, IRFU/Service d'Astrophysique, CEA Saclay, 91191 Gif-sur-Yvette, France

¹¹ Central Astronomical Observatory of RAS, Pulkovskoye Chaussee 65/1, 196140 St. Petersburg, Russia

¹² St. Petersburg State University, Universitetskij Pr. 28, 198504 St. Petersburg, Stary Peterhof, Russia

Received 15 July 2020 / Accepted 10 September 2020

ABSTRACT

Context. Investigating the dust heating mechanisms in galaxies provides a deeper understanding of how the internal energy balance drives their evolution. Over the last decade radiative transfer simulations based on the Monte Carlo method have emphasised the role of the various stellar populations heating the diffuse dust. Beyond the expected heating through ongoing star formation, older stellar populations (≥ 8 Gyr) and even active galactic nuclei can both contribute energy to the infrared emission of diffuse dust.

Aims. In this particular study we examine how the radiation of an external heating source, such as the less massive galaxy NGC 5195 in the M 51 interacting system, could affect the heating of the diffuse dust of its parent galaxy NGC 5194, and vice versa. Our goal is to quantify the exchange of energy between the two galaxies by mapping the 3D distribution of their radiation field.

Methods. We used SKIRT, a state-of-the-art 3D Monte Carlo radiative transfer code, to construct the 3D model of the radiation field of M 51, following the methodology defined in the DustPedia framework. In the interest of modelling, the assumed centre-to-centre distance separation between the two galaxies is ~ 10 kpc.

Results. Our model is able to reproduce the global spectral energy distribution of the system, and it matches the resolved optical and infrared images fairly well. In total, 40.7% of the intrinsic stellar radiation of the combined system is absorbed by dust. Furthermore, we quantify the contribution of the various dust heating sources in the system, and find that the young stellar population of NGC 5194 is the predominant dust-heating agent, with a global heating fraction of 71.2%. Another 23% is provided by the older stellar population of the same galaxy, while the remaining 5.8% has its origin in NGC 5195. Locally, we find that the regions of NGC 5194 closer to NGC 5195 are significantly affected by the radiation field of the latter, with the absorbed energy fraction rising up to 38%. The contribution of NGC 5195 remains under the percentage level in the outskirts of the disc of NGC 5194. This is the first time that the heating of the diffuse dust by a companion galaxy is quantified in a nearby interacting system.

Key words. radiative transfer – dust, extinction – galaxies: interactions – infrared: ISM – galaxies: individual: NGC 5194 – galaxies: individual: NGC 5195

1. Introduction

Galaxy interactions are extremely powerful mechanisms that drive the formation and evolution of galaxies in the Universe (Toomre & Toomre 1972; Toomre 1977; Somerville & Primack 1999; Kauffmann et al. 1999a,b; Springel et al. 2005). It is well known that interacting galaxies have higher dust and gas content than unperturbed galaxies (e.g. Combes et al. 1994; Casasola et al. 2004; Violino et al. 2018; Lisenfeld et al. 2019; Moreno

et al. 2019). Due to the strong tidal forces generated by such interactions, the redistribution and accumulation of baryonic matter (gas and dust inflows) in the interstellar medium (ISM) becomes possible, which triggers and/or enhances the formation of new stars (Kennicutt 1998; Kauffmann & Haehnelt 2000; Woods & Geller 2007). The interaction between galaxies may be even responsible, to some extent, for the variety of morphologies and morphological distortions that we observe. For example, numerical simulations strongly indicate that most elliptical

galaxies are the end product of galaxy merging (e.g. Toomre & Toomre 1972; Toomre 1977; Cox et al. 2006a,b; Naab & Trujillo 2006, and references therein).

Depending on the mass ratio of the involved galaxies, mergers are categorised as major or minor. The properties of mergers have been well studied, via observations (e.g. Woods & Geller 2007; Ellison et al. 2008, 2011, 2013; Weston et al. 2017) and via numeric simulations (e.g. Toomre & Toomre 1972; Barnes & Hernquist 1992, 1996; Mihos & Hernquist 1996; Di Matteo et al. 2007; Cox et al. 2008). Major mergers (i.e. galaxies of approximately equal mass) are responsible for the brightest objects in the local Universe, the ultraluminous infrared galaxies (ULIRGs), with bolometric luminosities greater than $10^{12} L_{\odot}$ (e.g. Sanders & Mirabel 1996; Clements et al. 1996; Dasyra et al. 2006). ULIRGs are characterised by enormous levels of ongoing star formation activity, but they are also heavily obscured by dust, emitting the bulk of their energy in the far-infrared (FIR) wavelengths. Moreover, the interactions between galaxies of unequal mass (i.e. minor mergers) are also an integral component of galaxy evolution, and could potentially lead towards an enhancement in star formation (Woods & Geller 2007). Kaviraj (2014) showcased the importance of minor mergers in the evolution of massive galaxies in the local Universe, with about half of the star formation activity driven by their merging process.

One of the most famous mergers in the local Universe is that of the grand design spiral arm galaxy NGC 5194 (M 51a, or the *Whirlpool* galaxy), and its companion, lenticular galaxy NGC 5195 (M 51b). The morphological type of M 51a is Sbc, and that of M 51b is SB0 (de Vaucouleurs et al. 1995). The centre of M 51a harbours a weak active galactic nucleus (AGN) classified as a Seyfert 2 (Terashima & Wilson 2001; Bradley et al. 2004), while M 51b is classified as a LINER (Satyapal et al. 2004; Moustakas et al. 2010). Usually, the term M 51 refers to NGC 5194 only, but in order to avoid confusion we will use M 51 to indicate the NGC 5194 + NGC 5195 interacting system (see Fig. 3 for an optical image of M 51). An open question that still remains today is whether or not the two galaxies had a single or multiple encounters. Evidence exists in support of either model, based on previous kinematic studies (Durrell et al. 2003; Salo & Laurikainen 2000), *N*-body simulations (Salo & Laurikainen 2000; Theis & Spinneker 2003), and hydrodynamic simulations (Dobbs et al. 2010). According to the single-encounter model, M 51b crossed M 51a about 300–500 Myr ago, and is currently located at a distance of 50 kpc beyond M 51a (Toomre & Toomre 1972). On the other hand, the dynamical models presented in Salo & Laurikainen (2000) are in favour of a multiple-encounter scenario, suggesting that after the first encounter 400–500 Myr ago, M 51b passed near M 51a for the second time about 50–100 Myr ago. This model places M 51b at a distance of 20 kpc beyond M 51a. Either way, at least one encounter occurred between the two galaxies, causing a burst of star formation 250–550 Myr ago in both of them (Tikhonov et al. 2009), and creating a stellar bridge that connects the galaxies. In this paper we adopt the multiple encounter scenario as the most up-to-date representation of M 51 in the literature that successfully explains the detailed kinematics based on HI radio observations (Salo & Laurikainen 2000), and because it is supported by *N*-body (Salo & Laurikainen 2000; Theis & Spinneker 2003) and hydrodynamic simulations (Dobbs et al. 2010).

The star formation in M 51a has continued until the present day and is ubiquitous across its disc (Tikhonov et al. 2009; Lee et al. 2011), while M 51b shows a deficiency in ionised gas (Thronson et al. 1991) and gravitationally stable molecular gas (Kohno et al. 2002), indicating the absence of ongoing

star formation. Yet recent radio observations claim otherwise, i.e. the process of star formation has returned to a low rate in the central region of M 51b (Alatalo et al. 2016). Tikhonov et al. (2009) determined the stellar composition of M 51b with optical colours, and found M 51b is surrounded by a significant number of asymptotic giant branch (AGB) stars, a result of the starburst 250–550 Myr ago. Furthermore, Mentuch Cooper et al. (2012) investigated the dust content of M 51, on spatial scales of ~ 1 kpc. The authors reported that a strong interstellar radiation field (ISRF) is heating the dust in M 51b to temperatures of ~ 30 K, and proposed three heating mechanisms, including heating from the evolved stellar population and from an AGN. Upon further investigation, both Eufrasio et al. (2017) and Wei et al. (2020) present evidence of an older stellar population (>5 Gyr) heating the dust in M 51b, by investigating the star formation history of M 51 on spatially resolved scales. Another way to probe the heating mechanisms is by constructing a 3D representation of the radiation field of M 51 and quantifying the various dust heating sources in the system.

Inverse radiative transfer simulations of face-on galaxies have now reached the point where they can be computationally efficient, and where they can provide all the necessary tools for a quantitative study of the mechanisms that power the infrared emission by dust, such as the different stellar populations (Viaene et al. 2017; Williams et al. 2019; Thirlwall et al. 2020; Verstocken et al. 2020; Nersesian et al. 2020) or other heating sources, such as AGN (Viaene et al. 2020). In a first attempt to quantify the dust heating fraction related to the star formation rate (SFR) in face-on spiral galaxies, De Looze et al. (2014) created a 3D radiative transfer model of M 51a (Paper I in this series of radiative transfer studies). They reveal that the contribution of the older stellar population (~ 10 Gyr) to the heating of the diffuse dust in the ISM is quite significant, donating up to 35% of its total energy budget to that cause. However, the authors of that study did not take into consideration the possible impact of M 51b to the spectral energy distribution of M 51a, which should be non-negligible due to their close relative distance (~ 20 kpc).

In this study, the fifth in the series, we revisit the radiative transfer model of M 51a (De Looze et al. 2014), and update the methodology of constructing such a model according to the pipeline established in Verstocken et al. (2020). Within the DustPedia framework (Davies et al. 2017) the method was optimised and applied to the early-spiral galaxy M 81 (Paper II, Verstocken et al. 2020) to a sample of face-on barred galaxies (Paper III, Nersesian et al. 2020) and to NGC 1068 which harbours an AGN (Paper IV, Viaene et al. 2020). Two additional studies employed our modelling strategy to build the models of the large Local Group galaxies M 31 (Viaene et al. 2017) and M 33 (Williams et al. 2019).

Due to its close proximity (~ 8 Mpc) and face-on views (inclination $i \sim 33$ deg), M 51 is a system of particular interest for investigating the dust heating mechanisms on spatially resolved scales across the infrared spectrum. The scope of the paper is to assess, possibly for the first time, the effect of the complex radiation field of an interacting pair of galaxies on the dust heating. We try to quantify the fraction of radiation by the different heating sources (e.g. old and young stellar populations, and M 51b) on spatial scales up to ~ 150 pc, by treating M 51 as a uniform system. With this study we want to provide a new way to quantify the typical exchange of radiation between the members of pre-mergers.

This paper is organised as follows. In Sect. 2 we describe the dataset used in this study, and the steps we followed to correct

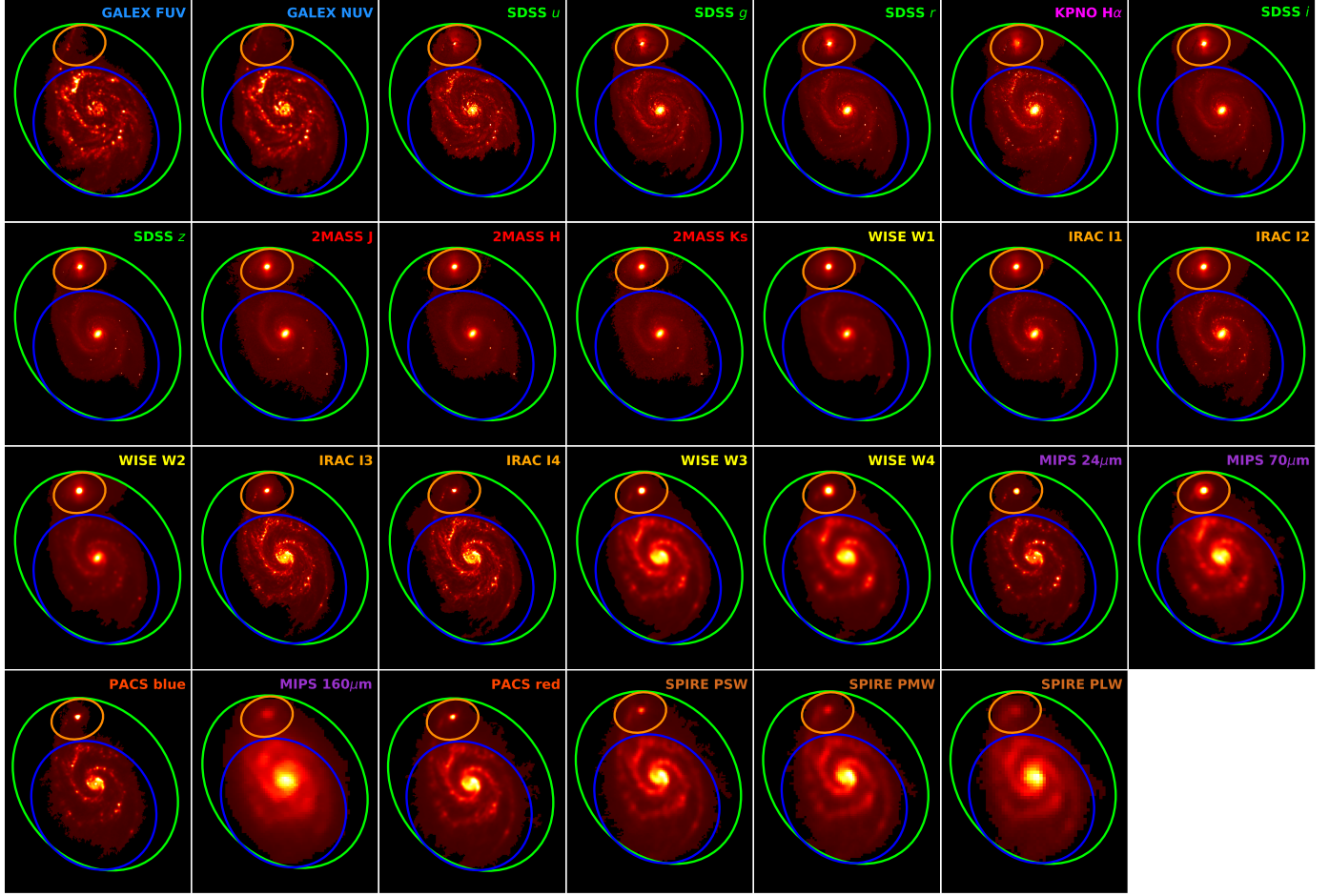


Fig. 1. Photometry thumbnail image grid for M 51. The green ellipse indicates the master aperture used for the determination of the integrated flux of M 51 and is centred on M 51a. The blue and orange ellipses indicate the regions used for the determination of the integrated fluxes of M 51a and M 51b, respectively.

the images for foreground stars and background noise. We also present the photometry and the results of a global SED fitting for M 51 with CIGALE. Section 3 briefly outlines our modelling approach, while in Sect. 4 we present and validate our results. In Sect. 5 we show how the contribution of the different stellar populations of M 51 shape its SED, and quantify their contribution to the dust heating. We investigate what the fraction of radiation related to M 51b is, and provide several maps of physical quantities. Various correlations and their discussion follow in Sect. 6. Our main conclusions are summarised in Sect. 7.

2. Dataset

2.1. Multi-wavelength imagery data

We acquired a total of 26 broadband images of M 51 from the DustPedia archive¹ (Davies et al. 2017; Clark et al. 2018). This panchromatic dataset covers a broad wavelength range from the far-ultraviolet (FUV) to the FIR domain (see Fig. 1), combining archival data from different ground-based and space telescopes: GALaxy Evolution eXplorer (GALEX; Morrissey et al. 2007), Sloan Digital Sky Survey (SDSS; York et al. 2000; Eisenstein et al. 2011), 2 Micron All-Sky Survey (2MASS; Skrutskie et al. 2006), Wide-field Infrared Survey Explorer (WISE; Wright et al. 2010), *Spitzer* (Werner et al. 2004); and *Herschel* (Pilbratt et al.

2010). The retrieved images are essential in our modelling, since they are used to construct the model and are directly compared to the simulated output images. An H α image of M 51 was downloaded from the SINGS (Kennicutt et al. 2003) database². The system was observed with the 2.1 m KPNO telescope, using a $2k \times 2k$ CCD which has a field of view (FOV) of $10'$, and a pixel scale of $0.305''$. The narrow-band filter at 6573 \AA was used, with an exposure time of 900 s. The stellar continuum was already subtracted from the image, with foreground stars being identified as negative point-like residual features. We removed those features by interpolating over the data. The final image has a photometric accuracy within 15%.

2.2. Foreground star identification

All images were pre-processed with a semi-automatic pipeline as was developed in PYTHON TOOLKIT for SKIRT³ (PTS⁴; Verstocken et al. 2020). First, we identify and exclude foreground stars in our images by searching the 2MASS All-Sky Catalog of Point Sources (Cutri et al. 2003). If the queried point sources have a local peak above a 3σ significance level, then they are identified as foreground stars and they are subtracted,

² <https://irsa.ipac.caltech.edu/data/SPITZER/SINGS>

³ http://www.skirt.ugent.be/root/_landing.html

⁴ http://www.skirt.ugent.be/pts8/_p_t_s.html

¹ <http://dustpedia.astro.noa.gr>

together with their neighbouring pixels, from the local background. The remaining features from the source subtraction are interpolated over the data, complemented with random noise. A manual inspection is performed afterwards for every image to ensure that none of the regions within the galaxy were identified as point sources by mistake. We applied this procedure for the GALEX, SDSS, $H\alpha$, 2MASS, WISE, and *Spitzer* images since the contribution from foreground stars in the *Herschel* bands is negligible.

2.3. Background subtraction and Galactic extinction

The next step in the pipeline is to correct the images for background emission and Galactic extinction. We define an elliptical region that encircles both galaxies and is centred on M51a (green ellipse in Fig. 1). In order to estimate the large-scale variation of pixel values around M51, we create a low-resolution background map with PHOTUTILS (Bradley et al. 2018), dividing each image into a mesh-grid of rectangular regions. Each region is a square box with a side of $6 \times FWHM$ of the particular image. All pixels inside the green ellipse associated with M51 are masked. The final background map and its standard deviation are then generated by interpolation of the low-resolution map within the central ellipse.

Finally, we correct all images that are affected by Galactic extinction. We obtain the V-band attenuation, A_V , from the IRSA Dust Extinction Service⁵ in order to determine the attenuation in the UV optical and near-infrared (NIR) filters. We assume an average extinction law in the Milky Way (MW) with $R_V = 3.1$ (Cardelli et al. 1989).

2.4. Global photometry

We perform our own global photometry, to ensure consistency over the measured flux densities between observed and mock images of M51. We drew three different elliptical regions, which are depicted in Fig. 1. We used a fixed aperture for all images and for each target case, while ensuring that the ellipses of M51a and M51b do not overlap. The process of generating the aperture ellipse of each target is described in Clark et al. (2018). The characteristics of each region are given in Table 1. We calculate the uncertainties by adding in quadrature the calibration uncertainty, and the mean variation from the background. The measured flux densities and uncertainties of the observed images are given in Appendix A. We note that the images of MIPS 70- and $160\mu\text{m}$, and their respective fluxes are not used in our modelling since the PACS 70- and $160\mu\text{m}$ images surpass them in spatial resolution. In total we use 25 images and the aperture photometry of M51 (green ellipse) to constrain our radiation transfer model. The photometry of the individual galaxies can be considered ancillary information, and it is only used to disentangle the IRAC $3.6\mu\text{m}$ flux density of the two galaxy components of the interacting pair.

According to previous studies (e.g. Toomre & Toomre 1972; Salo & Laurikainen 2000), the relative distance between the two galaxies is of the order of 20–50 kpc. In the interest of modelling, we adopted a common distance of $\sim 7.91 \pm 0.87$ Mpc (Sheth et al. 2010). The implications of this choice are discussed in Sect. 5.2. In addition, we estimate the inclination angles of M51a and M51b to be respectively 32.6 deg and 40.5 deg from a face-on view based on the method presented in Mosenkov et al. (2019). Finally, the position angles given in Table 1 are based on the values provided by Sheth et al. (2010).

2.5. SED fitting with CIGALE

During the last decade modelling the spectral energy distribution (SED) has become increasingly commonplace, and offers information about the global properties of any given galaxy (see Walcher et al. 2011; Conroy 2013; Baes 2020, for an overview of the available SED fitting tools and techniques). As a first attempt to extract the intrinsic properties of M51 and its galaxy components, we chose to fit their measured integrated fluxes with the SED fitting code CIGALE⁶ (Noll et al. 2009; Boquien et al. 2019). CIGALE is equipped with several modules, each one describing a different physical component. These individual modules can be combined to create a library of SED templates that will be fitted to the data. From these modules we use a flexible star formation history (SFH; Ciesla et al. 2016), Bruzual & Charlot (2003) simple stellar population (SSP) libraries, and a modified Calzetti et al. (2000) attenuation law. The Calzetti et al. (2000) starburst attenuation curve is combined with the Leitherer et al. (2002) curve between the Lyman break and 150 nm, to produce a flexible attenuation law that can be adapted on vastly different galaxies. For the dust emission we use The Heterogeneous Evolution Model for Interstellar Solids⁷ (THEMIS; Jones et al. 2013, 2017; Köhler et al. 2014) dust model. The THEMIS framework was built upon the optical properties of amorphous hydrocarbon and amorphous silicate materials as measured in the laboratory, and is qualitatively consistent with many dust observables, including the observed FUV-NIR extinction, and the shape of the IR to millimetre dust thermal emission. In order to fit the $H\alpha$ flux we used the low-resolution data as described in Boquien et al. (2019). For this study we adopted exactly the same parameter grid as in Nersesian et al. (2019, for details see their Table 1), with the only difference being that we used a Chabrier (2003) IMF instead of a Salpeter (1955), to be consistent with our radiation transfer modelling. The generated library includes over 80 million template SEDs. Finally, CIGALE adds in quadrature an extra 10% of the observed flux as model error.

Figure 2 shows the resulting best SEDs for all elliptical regions as defined in Table 1. The diamonds correspond to the 25 measured integrated luminosities for each elliptical region. The model SEDs match the observations closely and fall within the measured uncertainties. Comparing the SEDs of M51a (blue data) and M51b (orange data) in relation to the total emission of the system (green data), we find that most, if not all, of the UV and dust emission in M51 arises from M51a. The peak of the dust luminosity in the FIR from M51a is about one order of magnitude higher than the peak of dust luminosity in M51b. On the other hand, the SED of M51b is dominated by the optical and NIR emission of an older stellar population without any indication of strong, ongoing star formation activity.

This is further confirmed through the inferred SFRs from the global SED fitting. The SFR of M51b is about $0.026 \pm 0.023 M_\odot \text{ yr}^{-1}$. Interestingly enough, M51a forms stars at a moderate rate ($3.48 \pm 0.35 M_\odot \text{ yr}^{-1}$), which does not differ from SFRs measured in isolated galaxies. The stellar mass of M51a is estimated to be equal to $1.37 \pm 0.38 \times 10^{10} M_\odot$, and of M51b it is $1.35 \pm 0.26 \times 10^{10} M_\odot$. Therefore, M51 classifies as a major merger. The SFR of M51 is measured to be $3.30 \pm 0.41 M_\odot \text{ yr}^{-1}$, slightly lower than that of the subsystem M51a, but still consistent within the error bars. A possible explanation is that by incorporating the optical emission of M51b to the system, the ratio of UV-to-optical decreases, which results in a lower SFR. The total dust mass of the system is approximately

⁶ <https://cigale.lam.fr>

⁷ https://www.ias.u-psud.fr/themis/THEMIS_model.html

⁵ <https://irsa.ipac.caltech.edu/applications/DUST>

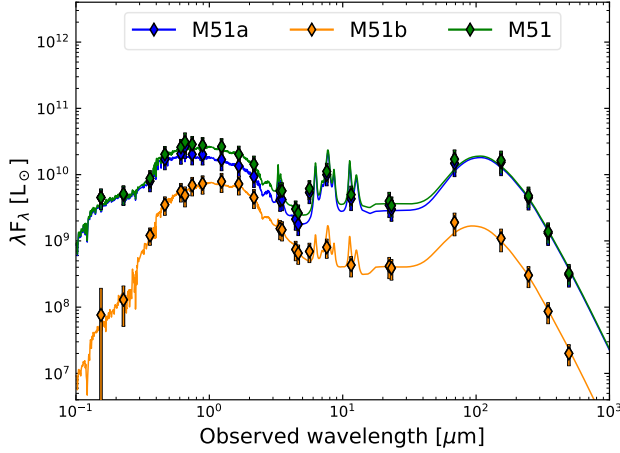


Fig. 2. SED of the M51 interacting pair with CIGALE. The green line is the best-fitting model of M51. The blue and orange lines are the best-fitting models of M51a and M51b, respectively. The inferred SEDs match the luminosities as measured from the aperture photometry shown in Fig. 1.

Table 1. Region definitions for the M51 interacting system.

Galaxy	RA (J2000) [deg]	Dec (J2000) [deg]	<i>a</i> [arcsec]	<i>b</i> [arcsec]	PA [deg]
M51a	202.4721	+47.175159	261.1	225.7	309.1
M51b	202.4981	+47.264645	100.4	76.14	14.3
M51	202.4697	+47.195199	357.4	288.1	309.1

Notes. Where *a* is the semi-major axis, and *b* is the semi-minor axis of a particular ellipse. PA is the position angle of the disc according to Sheth et al. (2010).

$3.40 \pm 0.65 \times 10^7 M_{\odot}$, while the attenuation in the FUV is 1.98 ± 0.15 mag. These quantities are representative of the interacting system and they will be used as normalisations of the various modelling components in our radiative transfer simulations.

3. Modelling approach

In order to build a 3D model for M51a and its companion, we follow the same strategy that was first introduced in De Looze et al. (2014), and later revised, and refined by Verstocken et al. (2020). We take advantage of the state-of-the-art radiative transfer code SKIRT (Baes et al. 2011; Camps & Baes 2015, 2020). SKIRT follows the Monte Carlo approach to simulate the physical processes of scattering, absorption, and thermal re-emission by dust, in different environments. SKIRT contains a large collection of geometries and geometry decorators (Baes & Camps 2015), grid structures (Saftly et al. 2013, 2014; Camps et al. 2013), and hybrid parallelisation techniques (Verstocken et al. 2017). In our model, we make use of two special classes in SKIRT: the ReadFitsGeometry and OffsetGeometryDecorator. The ReadFitsGeometry loads a given 2D map into SKIRT, and converts it into a 3D disc component through image de-projection and by applying a perfect exponential profile in the vertical direction (see De Looze et al. 2014). The OffsetGeometryDecorator adds an offset component or a 2D map, in our case the inclusion of the companion galaxy M51b, to the main geometry of M51a (Camps & Baes 2015, 2020).

In general, our model treats the two galaxies as a uniform system with multiple components. Table 2 gives an overview of the

Table 2. Overview of the modelling ingredients and normalisations for M51.

Component	Parameter	Value
M51a		
Old stellar population		
Bulge	<i>n</i>	0.995
	<i>q</i>	0.817
	<i>R_e</i> [pc]	621.1
Normalisation	<i>L_{bulge, 3.6}</i> [<i>L_⊙</i>]	0.54×10^9
Disc	2D geometry	IRAC 3.6 μm
	<i>h_{disc, z}</i> [pc]	390.8
Normalisation	<i>L_{disc, 3.6}</i> [<i>L_⊙</i>]	3.67×10^9
Young non-ionising stellar population		
Disc	2D geometry	GALEX FUV
	<i>h_{disc, z}</i> [pc]	195.4
Normalisation	<i>L_{yni, FUV}</i> [<i>L_⊙</i>]	2.15×10^{10}
Young ionising stellar population		
Disc	2D geometry	Hα + 0.031 × MIPS 24 μm
	<i>h_{disc, z}</i> [pc]	97.7
Normalisation	<i>L_{yi, FUV}</i> [<i>L_⊙</i>]	6.61×10^9
M51b		
Old stellar population		
Bulge	<i>n</i>	2.58
	<i>q</i>	0.564
	<i>R_e</i> [pc]	222.4
Normalisation	<i>L_{bulge, 3.6}</i> [<i>L_⊙</i>]	0.37×10^9
Disc	2D geometry	IRAC 3.6 μm
	<i>h_{disc, z}</i> [pc]	370.9
Normalisation	<i>L_{disc, 3.6}</i> [<i>L_⊙</i>]	1.11×10^9
M51		
Dust		
Disc	2D geometry	FUV attenuation map
	<i>h_{disc, z}</i> [pc]	195.4
Normalisation	<i>M_{dust}</i> [<i>M_⊙</i>]	3.40×10^7

Notes. The normalisations are the initial values in our parameter space, as derived from the CIGALE SED fitting of M51. Bulge parameters: *n* is the Sérsic index, *q* is the intrinsic flattening factor, and *R_e* is the effective radius.

parameters of each input geometry, while Fig. 3 illustrates an optical image of M51 with its various stellar and dust spatial distributions. Specifically for M51a, we assume four different stellar components and a thin disc of dust based on the standard geometric model of spiral galaxies (Xilouris et al. 1999; Popescu et al. 2000). The novelty of this study is that we complement our model with an extra stellar component, M51b. A common dust grid was generated that contains the dusty discs of both galaxies. The inclusion of M51b in the model will provide new insight into the interaction of the radiation field of a pre-merger, and will allow us to quantify, for the first time, the percentage of radiation from a neighbouring galaxy that goes into the dust heating of the main galaxy, and vice versa. In the following sections, we discuss briefly the different modelling components and highlight where we deviate from the parameterisation of De Looze et al. (2014). For a more complete description of our methodology we refer the reader to Verstocken et al. (2020).

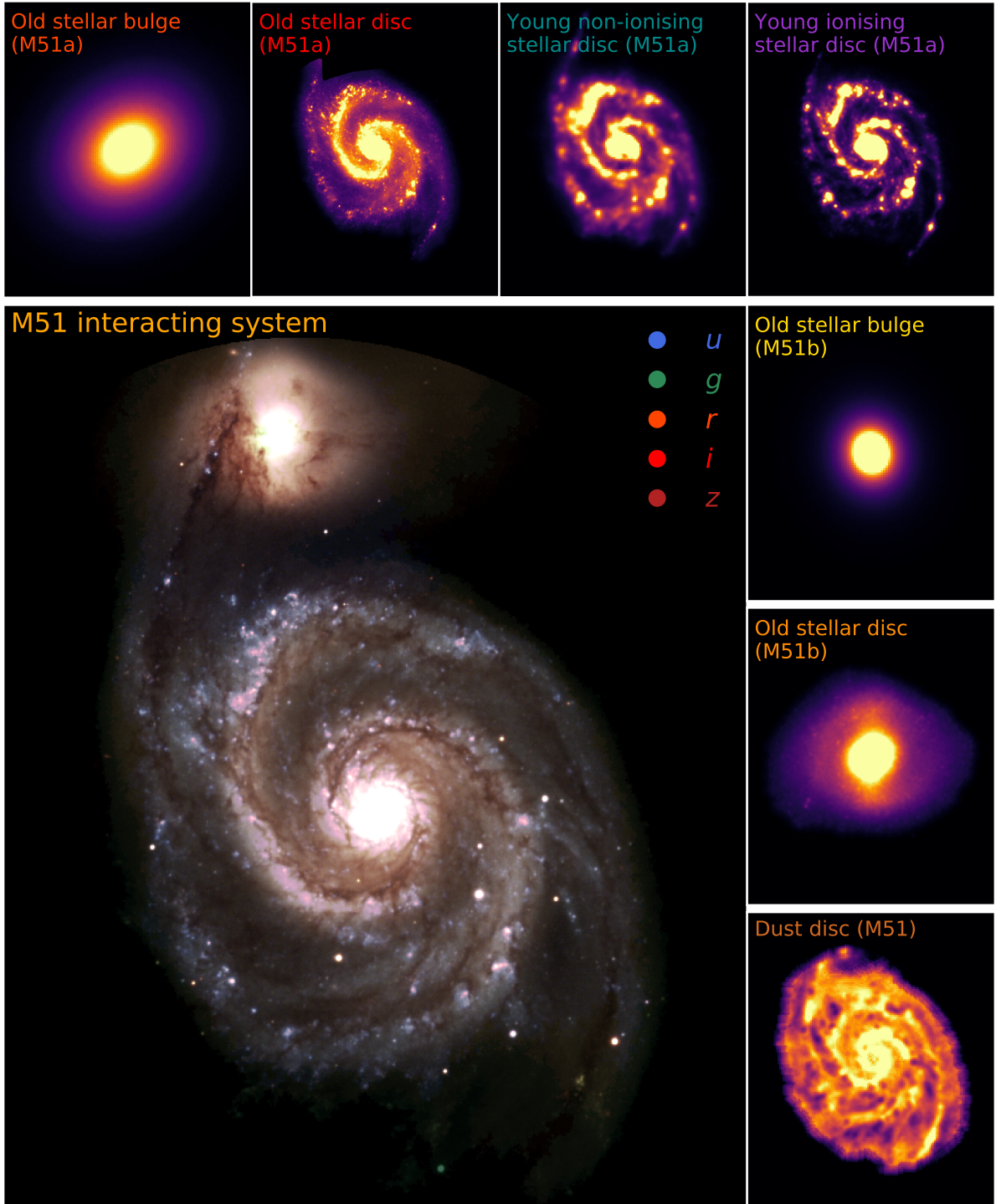


Fig. 3. Interacting system and components of M51. Main panel (*bottom left*): optical image of M51, created by combining the SDSS u, g, r, i, z images. Small panels (*top and right*): 2D representations of the various model components. *From left to right*: a zoomed-in view of M51a’s old stellar bulge, M51a’s old stellar disc, a yni stellar disc, and a yi stellar disc. *From top to bottom*: a zoomed-in view of M51b’s old stellar bulge, old stellar disc, and the combined dust distribution of M51a and M51b.

3.1. Stellar components of M51a

We used observational images at various wavelengths to describe the geometrical distribution of the different stellar components in M51a. We considered four stellar components, each one associated with a template SED and a 3D spatial geometry. The ages of each stellar component are in line with [De Looze et al. \(2014\)](#); however, in our analysis we use a [Chabrier \(2003\)](#) initial mass function (IMF) instead of a [Kroupa \(2002\)](#) IMF, and the [Bruzual](#)

& [Charlot \(2003\)](#) SSP templates instead of the [Maraston \(2005\)](#) SSP library.

The old stellar population is described by two components: an old stellar bulge and a disc. We used the *Spitzer* IRAC $3.6\,\mu\text{m}$ map, indicative of the older stars in the galaxy, to constrain this particular stellar population. However, the emission of the bulge and disc is entangled. Thus, a bulge-to-disc decomposition needs to be performed in order to retrieve the distribution of

the old stellar population in the disc. The bulge is modelled with a flattened Sérsic profile and a fixed luminosity. The decomposition parameters of the Sérsic geometry were taken from the S⁴G database⁸ (*Spitzer* Survey of Stellar Structure in Galaxies: Sheth et al. 2010; Salo et al. 2015). Then the old stellar population disc is obtained by subtracting the bulge from the total observed 3.6 μ m emission of M 51a. For this procedure it is assumed that the contamination from dust emission in the central region is negligible. The typical age of this stellar population is assumed to be ~ 10 Gyr with a fixed solar metallicity $Z = 0.02$ (as reported by Bresolin et al. 2004; Moustakas et al. 2010; Mentuch Cooper et al. 2012). The pixel scale resolution of the old stellar map is 0.75'' (or 28.75 pc at the distance of M 51).

The third stellar component is the young non-ionising (yni) stellar population in the disc with an assumed age of 100 Myr and a fixed solar metallicity $Z = 0.02$. The GALEX FUV image is best suited to constrain this stellar component since young stars (unobscured by dust) dominate this specific spectral range. We corrected the GALEX FUV map for dust attenuation by generating a FUV attenuation map based on the prescriptions of Cortese et al. (2008). These authors derive the FUV attenuation based on a polynomial function of the total infrared (TIR)-to-FUV ratio, on spatially resolved scales. The coefficients of the polynomial are determined for different values of the observed FUV- r colour. The TIR emission map is constructed from the MIPS 24 μ m, PACS 70 μ m, and PACS 160 μ m images, following the prescriptions described in Galametz et al. (2013). Consequently, after we convolve the FUV, FUV- r , and TIR maps to the PACS 160 μ m resolution (i.e. 4.0'' or 153.4 pc at the distance of M 51), we were able to retrieve the intrinsic FUV emission of the yni stellar population. Inspecting this map closely we find that the stellar bridge that connects the two galaxies is most prominent here.

The fourth and final stellar component is the young ionising (yi) stellar population, tracing the ongoing, obscured star formation. For this component we adopted the SED templates from MAPPINGS III (Groves et al. 2008) assuming an age of 10 Myr. To constrain its emission we combined the *Spitzer* MIPS 24 μ m image with the continuum-subtracted H α map, relying on the prescription derived by Calzetti et al. (2007). There are five parameters that define the MAPPINGS III templates, namely: the mean cluster mass (M_{cl}), the gas metallicity (Z), the compactness of the clusters (C), the pressure of the surrounding ISM (P_0), and the covering fraction of the molecular cloud photo-dissociation regions (f_{PDR}). We adopted the following parameters as our default values and according to De Looze et al. (2014): $Z = 0.02$, $M_{cl} = 10^5 M_{\odot}$, $\log C = 5.5$, $P_0/k = 10^6 \text{ K cm}^{-3}$, and $f_{PDR} = 0.2$. The corresponding maps of the two young stellar populations were corrected for the emission originating from old stars by subtracting a scaled version of the 3.6 μ m image (Verstocken et al. 2020, and references therein). The pixel scale resolution of the yi stellar map is 1.5'' (or 57.5 pc at the distance of M 51).

3.2. Stellar component of M51b

The lack of major ongoing star formation in M51b led us to assume that all of its stellar radiation stems from an older stellar population. In addition, the bulge of the galaxy is very bright in the optical and NIR wavelengths (see Fig. 1), which could cause a strong elongated feature in the simulated images through the de-projection of the input map. In order to diminish the effect of

this feature we replace the bulge with an analytical density profile. The bulge is modelled with a Sérsic profile, the parameters of which are given by the S⁴G database (Sheth et al. 2010; Salo et al. 2015). Through a bulge-to-disc decomposition we subtract the emission of the bulge from the IRAC 3.6 μ m image in order to get the stellar emission in the disc. The total luminosity is fixed such that it corresponds to the total IRAC 3.6 μ m luminosity of M 51b. We assumed that the stellar age and metallicity of M 51b are similar to those of M 51a, that is ~ 10 Gyr with a fixed solar metallicity $Z = 0.02$ (see also Lee et al. 2012), while we adopted a Chabrier (2003) IMF and the Bruzual & Charlot (2003) SSP templates. Finally, we assume that the overall contamination by the emission of aromatic features in the 3.6 μ m is negligible, since Boulade et al. (1996) found that their emission is concentrated on the central region of M 51b (≤ 80 pc). The pixel scale resolution of the old stellar component of M 51b is 0.75'' (or 28.75 pc at the distance of M 51).

3.3. Dust component of M51

The dust component is the combination of the thin dusty disc of M 51a and the dusty nucleus of M 51b. The diffuse dust disc is constrained through the FUV attenuation map, while the dust around the star-forming regions is modelled through a subgrid that relies on the MAPPINGS III SED templates. The advantage of using the FUV attenuation map is that we can trace the cold diffuse dust at higher spatial resolution than if we had used the images at longer wavelengths (e.g. SPIRE 500 μ m), which are less sensitive to the dust temperature and their resolution is significantly worse. Another difference between the modelling setup of De Looze et al. (2014) and ours is that for the dust composition we used the DustPedia reference dust model THEMIS (Jones et al. 2013, 2017; Köhler et al. 2014) instead of a Draine & Li (2007) dust mixture. The adopted THEMIS model is for the MW diffuse ISM, and we assume a constant fraction of aromatic hydrocarbons throughout the disc. As shown in the bottom right panel of Fig. 3, the dust map highlights nicely the complex spiral structure of M 51a, but also reveals that any significant amount of dust in M 51b is concentrated in the vicinity of its central regions. The SDSS image also shows some strong dusty features along the tidal bridge and in the foreground of M 51b; however, they are not resolved in the *Herschel* bands. The pixel scale resolution of the dust map is 4.0'' (or 153.4 pc at the distance of M 51).

3.4. Including the 3D feature

Using the ReadFitsGeometry class in SKIRT allows the construction of complex 3D geometries from 2D maps, ensuring that the flux density is conserved during the conversion from 2D to 3D (De Looze et al. 2014). To create the 3D distribution of the disc components, we assigned to each component an exponential profile of different scale heights, h_z , based on previous estimates of the vertical extent of edge-on galaxies (De Geyter et al. 2014). Specifically, De Geyter et al. (2014) found a mean ratio of scale length to scale height of 8.26. The scale lengths of M 51a and M 51b were obtained from the S⁴G database, and subsequently we computed a scale height of 390.8 pc for the old stellar disc of M 51a, and 370.9 pc for the old stellar disc of M 51b. The yni and dust discs share the same scale height (i.e. one-half of the scale height of the old stellar population of M 51a), while the scale height of the yi stellar disc is one-quarter that of the old stellar disc of M 51a (De Looze et al. 2014; Viaene et al. 2017; Verstocken et al. 2020). Each 2D map is de-projected on a face-on view (i.e. $i = 0$ deg), and then it is smeared out in the vertical direction according to the given exponential profile.

⁸ https://www.oulu.fi/astronomy/S4G_PIPELINES4/MAIN

3.5. Setup of the *skirt* simulations

Due to the inherent geometrical complexity of the system, a few simplifying assumptions needed to be made. One simplification was that M51b has the same inclination angle as M51a ($\sim 33^\circ$). Another simplification was to assume that both galaxies are located in the same plane. Although, this assumption does not represent the current status of their relative distance separation, which according to the multiple encounter model is approximately 20 kpc, it certainly did 50–100 Myr ago during the passage of M51b near M51a (Salo & Laurikainen 2000). We discuss the implications of this assumption to the contribution of dust heating by M51b in Sect. 5.2.

We generated a k - d dust grid (Saftly et al. 2014) based on the dust distribution of M51, through which the photons of both galaxies will propagate in our simulations. The grid was made in a hierarchical way by splitting the spatial domain into 3D cells (voxels). The $x \times y \times z$ dimensions of the grid structure are $26.3 \times 26.3 \times 3.9 \text{ kpc}^3$, containing approximately 1.4 million dust cells. The cell sizes were adjusted to the dust density distribution of M51; grid cells are small where locations require high resolution, whereas cells can be much bigger elsewhere. The subdivision for individual cells stops when they contain a dust mass fraction below 8×10^{-7} . The size of a particular dust cell varies from 102 pc (maximum spatial resolution) to 3 kpc. Finally, we simulate datacubes of the observed radiation with a pixel scale of $4.0''$ or 153.4 pc.

3.6. χ^2 optimisation

The normalisations assigned to each stellar and dust component in Table 2 act as initial guess values and they were set as free parameters, determined through our optimisation procedure (Verstocken et al. 2020). The IRAC $3.6 \mu\text{m}$ luminosities of M51a's old stellar bulge and M51b, were kept fixed a priori. In total, we left four parameters in our model free, namely the FUV luminosity of the yni stellar disc ($L_{\text{yni}, \text{FUV}}$), the FUV luminosity of the yi stellar disc ($L_{\text{yi}, \text{FUV}}$), the IRAC $3.6 \mu\text{m}$ luminosity of the old stellar disc ($L_{\text{old}, 3.6}^{\text{disc}}$), and the total dust mass (M_{dust}). The $L_{\text{yi}, \text{FUV}}$ was calculated by converting the SFR, derived from CIGALE, into a spectral luminosity. This was done by generating the Groves et al. (2008) spectrum and scaling it to the SFR. Then the $L_{\text{yni}, \text{FUV}}$ was obtained by correcting the observed FUV luminosity with the FUV attenuation value retrieved by CIGALE, and then subtracting the found $L_{\text{yi}, \text{FUV}}$.

We would like to note that the $L_{\text{old}, 3.6}^{\text{disc}}$ was set as a free parameter to disentangle the light contamination by M51b, and the possible dust contamination by the $3.3 \mu\text{m}$ aromatic feature. Global luminosities are distributed on the voxels according to the density distributions as prescribed by the physical maps. In order to determine the best model from our radiative transfer simulations, we followed a two-step minimisation procedure. The optimisation scheme was constructed in such a way so that it can reduce the computational cost of our simulations.

The first phase of the optimisation is to explore the parameter space around the initial guess values. To this end, we define a broad grid in the 4D parameter space of ($L_{\text{yni}, \text{FUV}}$, $L_{\text{yi}, \text{FUV}}$, $L_{\text{old}, 3.6}^{\text{disc}}$, M_{dust}). For each free parameter we consider five grid points totalling 625 simulated SEDs. Furthermore, we adopt a low-resolution spectrum of 115 wavelengths (0.1 – $1000 \mu\text{m}$), which includes the effective wavelength of each band in our dataset for a direct comparison to the observed flux densities. At this stage we do not require the spectral convolution of the sim-

ulated fluxes and images to the filter response curves. To ensure a satisfactory reconstruction of the global SEDs, we sample the emitted light in each wavelength with a sufficient number of photon packages (10^6). Moreover, we define six basic wavelength regimes, UV, optical, NIR, mid-infrared (MIR), FIR, and sub-millimetre (submm), in order to assign a specific weight to each broadband filter, such that each wavelength regime is of equal importance (Viaene et al. 2017; Verstocken et al. 2020). The best-fitting model is determined through the comparison of the global observed and modelled SEDs:

$$\chi^2 = \sum_X w_X \left(\frac{F_X^{\text{obs}} - F_X^{\text{sim}}}{\sigma_X^{\text{obs}}} \right)^2. \quad (1)$$

Here w_X , F_X^{obs} , F_X^{sim} , and σ_X^{obs} are the assigned weight factor, global observed flux density, mock flux density, and observed error corresponding to waveband X , respectively. Then we use the derived best-fitting values of this first exploratory stage to narrow down the possible ranges of our 4D parameter grid, and to generate a new refined parameter grid space for the second round of simulations.

For the second stage of the optimisation procedure, we define a high-resolution spectrum of 222 wavelength points, and shoot 5×10^6 photon packages per wavelength to ensure a realistic representation of the physical processes of emission, absorption, and scattering in M51. Again, we use five grid points for each free parameter (625 simulated SEDs), while the option of spectral convolution is now enabled. The output of each simulation includes the SED of M51 and a set of broadband images that can be directly compared to the observed images. In contrast to De Looze et al. (2014), who optimised only the global fluxes, we compute the χ^2 metric based on the pixel-by-pixel difference of observed versus mock images in each band:

$$\chi^2 = \sum_X \sum_p w_X \left[\frac{\mu_X^{\text{obs}}(p) - \mu_X^{\text{sim}}(p)}{\sigma_X^{\text{obs}}(p)} \right]^2. \quad (2)$$

Here the first summation covers all filters X for which data are available; the second sum loops over all pixels p in the image corresponding to band X . The quantities $\mu_X^{\text{obs}}(p)$, $\mu_X^{\text{sim}}(p)$, and $\sigma_X^{\text{obs}}(p)$ are the observed surface density, mock surface density, and observed error in pixel p of band X , respectively. Finally, w_X is again the assigned weight factor given to band X .

We ran our simulations on the high-performance cluster of Ghent University. Each simulation of the first batch was evaluated under 50 min (on average) on a 12 CPU node. For the second batch of high-resolution simulations, the average time needed for each simulation to finish was about 4 h, again, on a 12 CPU node.

4. Model results

In the section that follows, we present the radiative transfer model that was best fit to the panchromatic dataset of M51. We show the best-fitting SED along with the SEDs of the different stellar components, and we validate our results through an image comparison between the observed and the simulated images of M51.

4.1. SED fitting with *skirt*

Once the best-fitting model is determined from our optimisation procedure, we run another simulation of that model, but

with twice the number of photon packages (10^7 photon packages) per wavelength (222 wavelengths in total). This is done in order to reduce the inherent Monte Carlo noise and to generate high-quality images of M51. In addition, we set individual simulations for each stellar component using the same dust grid configuration. This enables us to measure the pure fraction of radiation that is absorbed and/or scattered by the dust cells for each stellar source, and to examine their effective dust heating range.

The radiative transfer model with the lowest local χ^2 has

$$\begin{cases} L_{\text{old}, 3.6}^{\text{disc}} = (2.08 \pm 0.43) \times 10^9 L_{\odot} \\ L_{\text{yni}, \text{FUV}} = (1.51 \pm 0.37) \times 10^{10} L_{\odot} \\ L_{\text{yi}, \text{FUV}} = (0.64 \pm 0.29) \times 10^9 L_{\odot} \\ M_{\text{dust}} = (5.09 \pm 0.83) \times 10^7 M_{\odot}. \end{cases} \quad (3)$$

The uncertainties on the parameter values were estimated by their probability distribution functions. In general, these parameters are in a good agreement with the initial guess values derived from the 1D SED fitting with CIGALE (see normalisations in Table 2). Specifically, the most probable luminosities by the radiative transfer model are below the initial guess, with the most deviant case being for $L_{\text{yi}, \text{FUV}}$. The model luminosity of the yi stellar population is lower by 1.0 dex. On the other hand, the model predicts a dust mass that is approximately 1.5 times higher than that derived by CIGALE. It appears that the differences in $L_{\text{yi}, \text{FUV}}$ and M_{dust} are linked. The model prefers adding more diffuse dust over a higher ionising radiation, required to warm up the dust in PDRs.

In Fig. 4 we present the SED of the best-fitting model for M51 along with its observed counterpart. The different coloured lines correspond to the SEDs of the various stellar components of M51a, and to the contribution of M51b to the total SED. Due to the non-linear dependence between the absorbed energy and thermal re-emission by dust, summing up the individual SEDs does not result in the total model SED (black line). Furthermore, the dust emission of each SED component corresponds to the total absorbed radiation, re-processed by dust, in both galaxies. Overall, the comparison of the observations and the mock luminosities reveals an exceptionally good agreement between the two, with absolute differences not exceeding 0.26 dex.

In detail, our model does a fine job fitting the UV, optical, NIR, and MIR (up to $4.6 \mu\text{m}$) regions of the spectrum, with absolute differences below 0.1 dex. However, we note one significant deviation in the near-ultraviolet (NUV) band ($0.23 \mu\text{m}$), with the model underestimating the NUV luminosity by 0.16 dex. A similar deviation was observed in the radiative transfer model of M51a by De Looze et al. (2014), but with a higher difference (about 0.3 dex). The NUV band still remains one of the hardest bands to model due to its dependence on the various components, and because the effects of dust extinction are more pronounced at this wavelength range (Decleir et al. 2019). Another major discrepancy is seen for the 2MASS K_s band ($2.16 \mu\text{m}$). Surprisingly, our model underestimates the luminosity by 0.21 dex, even though it perfectly matches the emission in the 2MASS J and H wavebands (less than -0.01 dex). Recalling the imagery data of Fig. 1, it is evident that the 2MASS images are less sensitive to the faint stellar emission. Consequently, the model struggles to properly sample the diffuse stellar emission in this particular wavelength range, resulting in the lower luminosity for the 2MASS K_s band. This difference could also be related to thermally pulsating asymptotic giant branch (TP-AGB) stars which have a dominant contribution at those wavelengths, and

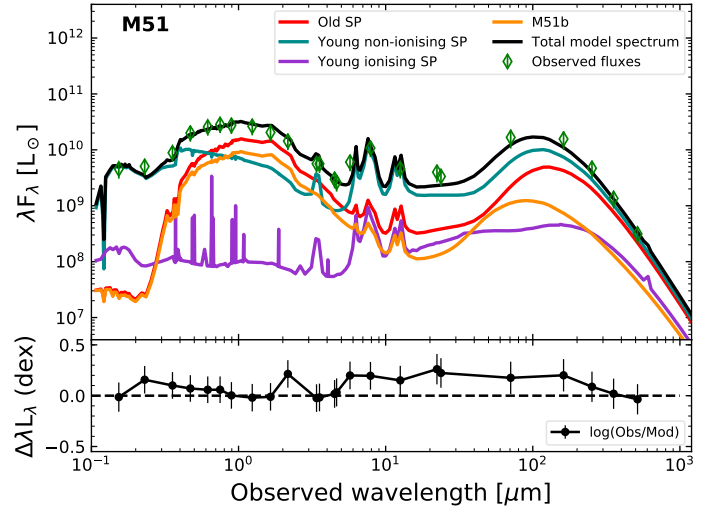


Fig. 4. *Top panel:* panchromatic SED of M51. The black line is the best-fitting radiative transfer model, run at high-resolution. The green diamonds are the observed broadband luminosities of M51 (see Table A.1). The red, cyan, and violet lines represent the SEDs for simulations with only the stellar components of M51a: old, young non-ionising, and young ionising stellar population, respectively. The orange line represents the SED of M51b. The dust component, which includes the dusty discs of both galaxies, is still present in these simulations. *Bottom panel:* difference in dex values between the observations and the mock luminosities.

whose evolution is not well understood. Finally, the mismatch between model and observations could also be related to the specific choice of stellar libraries (and their inability to model the TP-AGB evolution correctly).

Beyond $4.6 \mu\text{m}$ our model underestimates the emission of the aromatic feature carriers observed in the IRAC I3 ($5.8 \mu\text{m}$), IRAC I4 ($8 \mu\text{m}$), and WISE W3 ($12 \mu\text{m}$), as well as the continuum emission in the 22– $24 \mu\text{m}$. The largest deviation in our model is for the WISE W4 ($22 \mu\text{m}$) emission, with a difference of 0.26 dex. The model of M51a by De Looze et al. (2014), similarly underestimated the dust emission at these wavelengths. The cause of this discrepancy appears to be associated with our assumption of a constant fraction of hydrocarbons throughout the system, as it is shown that the fraction of hydrocarbons varies within galaxies and from galaxy to galaxy (Galliano et al. 2008; Peeters et al. 2017). In low-density regions, dust grains are prone to destruction by the intense stellar radiation field (e.g. Draine et al. 2007; Bendo et al. 2008; Galliano et al. 2018), whereas in high-density regions dust carriers may grow onto bigger grains through accretion and coagulation (e.g. Hirashita & Kuo 2011; Köhler et al. 2012, 2015). Unfortunately, these processes cannot be taken into account as they have not been incorporated in SKIRT yet; however, the framework to implement them is now ready (Camps & Baes 2020). Finally, the model falls short fitting the peak of the dust emission in the FIR (the difference in PACS 70 and $160 \mu\text{m}$ is 0.18 dex and 0.2 dex, respectively), while the luminosities of the longest FIR wavelengths ($\geq 250 \mu\text{m}$) are in excellent agreement, with residuals below 0.1 dex. As we already mentioned, the small offset between the observed and model dust emission peak indicates that more UV radiation was needed to warm up the dust.

Looking now at the individual component SEDs, it is evident that the yni stellar population (cyan line), of an assumed age of 100 Myr, is the dominant UV source in M51a. The yni stars are also responsible for the bright aromatic features observed at 3.3,

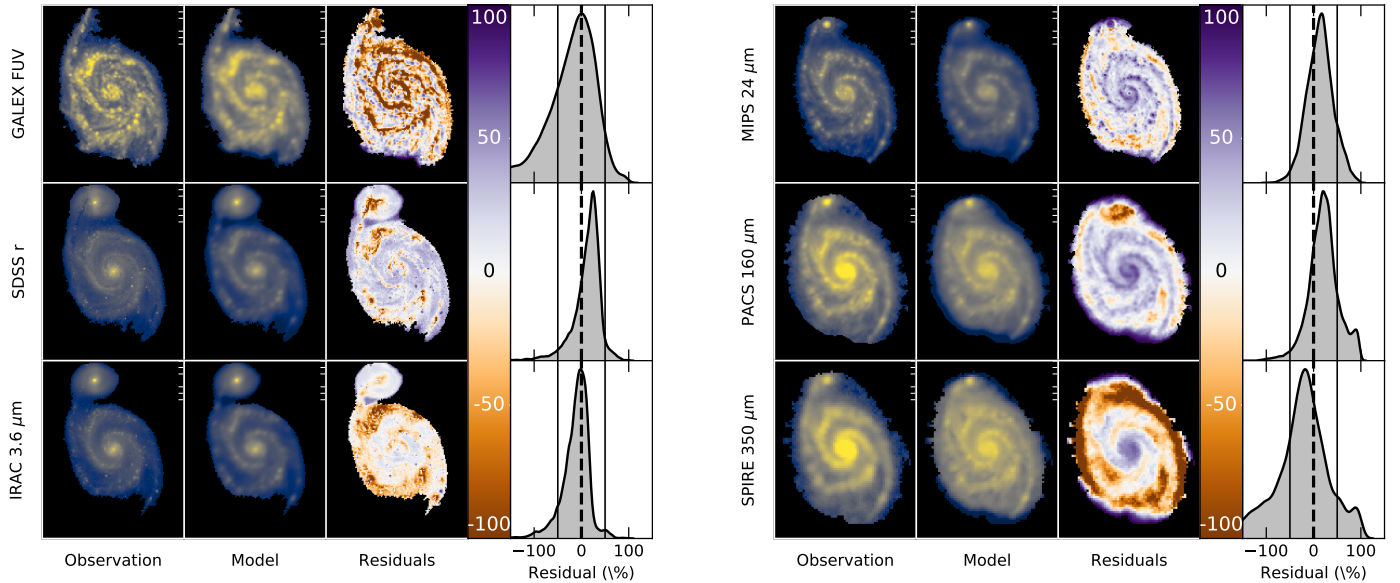


Fig. 5. Comparison of the simulated images with observations in selected wavebands for M51. *First column:* observed images; *second column:* simulated images; *third column:* residuals maps between observed and simulated images ($F_{\nu, \text{obs}} - F_{\nu, \text{mod}} / F_{\nu, \text{obs}}$). Positive values (in blue) mean that the model underestimates the observed emission, and negative values (in red) mean that the model overestimates the observations. *Last column:* KDE distributions of the residual pixel values. The simulated images have the same pixel mask as the observed images. The colour-coding of the first two columns reflects a normalised flux density. The selected wavebands are GALEX FUV, SDSS r , IRAC $3.6\,\mu\text{m}$, MIPS $24\,\mu\text{m}$, PACS $160\,\mu\text{m}$, and SPIRE $350\,\mu\text{m}$. The vertical lines indicate the 0 (dashed line) and ± 50 (solid lines) percentage levels of the residuals.

6.2, 8, and $11.3\,\mu\text{m}$. According to the THEMIS dust model, these features are due to amorphous hydrocarbon solids (Jones et al. 2013, 2017; Galliano 2018). The bulk of the dust emission in the FIR is also provided through heating by the same stellar population. Furthermore, the lack of a strong ionising stellar component in the disc (violet line) could explain the underestimation of the MIR and FIR dust emission. It can further explain the surprisingly low $L_{\nu, \text{FUV}}$ since this parameter was used to constrain this particular SED. On the other hand, we see that M51b provides a significant contribution to the optical and NIR emission in the system. The absorbed and/or scattered radiation from M51b warms up its own dust, and a considerable fraction of the diffuse dust of M51a, to high dust temperatures. This can be clearly seen from the dust emission induced by the companion galaxy, the peak of which is shifted toward a shorter wavelength, indicative of a warmer dust component.

4.2. Image comparison

Since the simulated images were used in the optimisation procedure to determine the best-fitting model, it is relevant to present a spatial comparison between the model and the observed broadband images. The spectral convolution of the simulated datacube generates a set of 24 mock images, all clipped to the same signal-to-noise mask of their observed counterpart. Figure 5 illustrates the spatial comparison for a few selected broadband images, characteristic of the different wavelength regimes (UV, optical, NIR, MIR, FIR, submm). The first column shows the observations, the second column the simulations, and the third column the residual images. The fourth column of Fig. 5 shows the kernel density estimation (KDE) of the residual values.

The visual inspection of the residual images presented here reveals the excellent agreement between model and observations for M51, with the majority of the model pixels within $\pm 50\%$ of the observed counterparts. A substantial fraction of these residuals is caused by the soft blur that is visible in the model images,

a relic of the de-projection procedure. In the FUV band the model image compares quite well with the observation, with the KDE distribution of the residuals peaking near 10%. The model is able to correctly reproduce the diffuse FUV emission in the inter-arm regions of the disc, yet it overestimates the emission across the spiral arms with residuals lower than -50% . De Looze et al. (2014) also found a similar result in their model of M51a. They explained these variations in their model as a result of the assumed constant age of the young stellar populations. In reality, we expect that spiral arms are populated by stellar clusters of different ages (see also Wei et al. 2020). In addition, the model overestimates the emission from the bulge of M51b by up to 90%.

A very good match between model and observation is seen also for the optical image in the SDSS r band. The model accurately reproduces the observed image, with a narrow distribution and a peak at residual values close to 23%. Very few residuals are below 0% and they are located in the spiral arm nearest to the companion galaxy and in the tidal bridge. Likewise, the IRAC $3.6\,\mu\text{m}$ residual map has a narrow distribution with a peak slightly shifted below 0%. The map itself shows very few residuals, remaining mostly close to the interaction region and partially in the inner regions of the spiral arms. The diffuse old stellar emission and the emission from the bulge of each galaxy are well reproduced. With respect to the IRAC $3.6\,\mu\text{m}$ image produced by De Looze et al. (2014), the diffuse stellar emission was underestimated by 30%. Our improved spatial reconstruction of the IRAC $3.6\,\mu\text{m}$ image makes us confident that the old stellar population (i.e. the stellar mass in the interacting system) is accurately described by our model.

Despite the considerable difference found in the integrated MIPS $24\,\mu\text{m}$ luminosity (0.22 dex or 40.2%), the model accurately describes the spatially resolved diffuse emission from warm dust in the disc and inter-arm regions of M51a. The pixel values in the simulated image are underestimated by 14.5%, with the spiral structure being quite prominent in the residual map.

Specifically, the model fails to reproduce the sites of obscured star formation across the spiral arms with the relative differences exceeding 50%. The bright centre of M 51b is also heavily underestimated (up to 85%), while the footprint of the MIPS 24 μ m PSF adds up to the observed discrepancies. The FIR simulated images and observations are in good agreement, with residual values having a narrow distribution peaking within $\pm 22\%$. In the case of PACS 160 μ m waveband, the model underestimates the dust emission mainly in the spiral arms and the central region of M 51a, with the diffuse dust in the inter-arm regions accurately represented. The MIPS 24 μ m and PACS 160 μ m images are better reproduced in the model of De Looze et al. (2014), where the peak of the residual distribution for these two bands is very close to 0%.

Finally, the SPIRE 350 μ m emission in the disc, a tracer of the cold diffuse dust, is overestimated by up to 22%. The centre of M 51a is underestimated with the relative residuals increasing to 55%, while the edges of the disc are greatly overestimated. Arguably, our simplification of placing M 51a and M 51b at the same distance from the observer, combined with the lower dust density around the edges of the disc, allowed the photons of the companion galaxy to propagate through those regions, warming up the colder dust component (see also Sects. 5.1 and 5.3). The same explanation applies to the conspicuous feature in the PACS 160 μ m residual map around the region where the two galaxies blend in.

In conclusion, despite small deviations, we are confident that our radiative transfer model of M 51 describes the observed data sufficiently. Compared to the model of M 51a by De Looze et al. (2014), our model does a better job of reconstructing the short wavelength images (UV, optical, NIR), while it deviates for the longer wavelengths (MIR and FIR). The differences between the two models appear to be connected to some extent with the chosen dust mixture properties (THEMIS versus Draine & Li 2007). For example, the total dust mass we obtained for M 51 is $\sim 34\%$ lower than the dust mass $M_{\text{dust}} = 7.7 \times 10^7 M_{\odot}$ reported by De Looze et al. (2014) just for M 51a. This is expected, since the dust in THEMIS is more emissive than in the Draine & Li (2007) model, having both a lower emissivity index β and a higher absolute opacity κ_0 value (e.g. Fig. 4 of Galliano et al. 2018). The inclusion or not of the companion galaxy is an important factor as well. The introduction of this extra component in our model certainly helped to better sample the diffuse stellar emission in the optical and NIR wavebands. On the other hand, it resulted in the significant overestimation of the cold diffuse dust emission around the edges of M 51a. The direct influx of photons, by M 51b, could explain the extra amount of dust emission. We keep in mind these caveats when analysing the dust heating in Sect. 5.1.

5. Dust heating results

Cosmic dust has a major influence on how we observe galaxies since it is responsible for the reddening and scattering of starlight. Several studies have shown that dust can absorb roughly one-third of the total stellar radiation, in some cases even more than one-half, in nearby late-type galaxies (e.g. Viaene et al. 2016; Bianchi et al. 2018, and references therein). Based on the energy-balance principle, the stellar electromagnetic energy absorbed by dust is then re-processed and released in the form of thermal radiation at MIR, FIR, and submillimetre wavelengths. We measure the global dust heating fraction simply by calculating the fraction of dust to bolometric luminosity: $f_{\text{abs}}^{\text{SKIRT}} = L_{\text{dust}} / (L_{\text{stars}} + L_{\text{dust}})$. The parameter L_{stars} is the total observed

stellar emission and L_{dust} is the total dust luminosity, computed by integrating the SED presented in Fig. 4. For M 51 we find that 40.7% of its total stellar radiation is absorbed by dust. A similar value of 41.2% is retrieved from the global SED of M 51 as derived with CIGALE (see Fig. 2). The advantage of a 3D radiative transfer model of M 51 over a simple 1D SED fitting is that we can disentangle the dust-heating fraction by the different stellar components not only on global scales but also on resolved sub-kpc scales. Another advantage is that we can quantify the dust-heating fraction related to the companion galaxy, M 51b. In the following sections, we present the dust-heating fractions by the different stellar sources in our model, as well as the intrinsic properties and correlations for each galaxy in the interacting system.

5.1. Heating maps

Each dust cell in our simulation holds information about the energy it absorbed and its origin. Subsequently, it is possible to disentangle the complex radiation field of the interacting system and quantify the dust-heating fraction from the different heating agents. We define the young heating fraction, denoted f_{young} , as the fraction originating from the yni and yi stellar populations of M 51a; likewise, we define the old heating fraction, denoted f_{old} , as the heating fraction provided by the old stellar population of M 51a. The heating fraction related to the absorbed radiation emitted by M 51b across the galactic disc of M 51 is denoted f_{M51b} . We obtain these heating fractions through

$$\begin{aligned} L_{\text{tot}}^{\text{abs}} &= L_{\text{old}}^{\text{abs}} + L_{\text{yni}}^{\text{abs}} + L_{\text{yi}}^{\text{abs}} + L_{\text{M51b}}^{\text{abs}}, \\ f_{\text{old}} &= \frac{L_{\text{old}}^{\text{abs}}}{L_{\text{tot}}^{\text{abs}}}, \\ f_{\text{young}} &= \frac{L_{\text{yni}}^{\text{abs}} + L_{\text{yi}}^{\text{abs}}}{L_{\text{tot}}^{\text{abs}}}, \\ f_{\text{M51b}} &= \frac{L_{\text{M51b}}^{\text{abs}}}{L_{\text{tot}}^{\text{abs}}}, \end{aligned} \quad (4)$$

where $L_{\text{tot}}^{\text{abs}}$ is the total stellar luminosity absorbed by dust for the interacting pair, $L_{\text{yni}}^{\text{abs}}$ and $L_{\text{yi}}^{\text{abs}}$ are respectively the luminosities of the yni and yi stellar populations absorbed by dust, and $L_{\text{M51b}}^{\text{abs}}$ is the absorbed luminosity originally emitted by M 51b.

Figure 6 shows the various dust-heating fractions from a face-on view of M 51. The left and middle panels show the dust-heating maps for the old and young stellar populations, respectively. The right panel depicts the dust-heating fraction provided by the older stellar population in M 51b. This particular heating map is in log-scale in order to better visualise the heating fractions across the disc of M 51a. These maps are averaged along the line of sight. Figure 6 also shows the positions of the 3 kpc and 8 kpc radii, and the limits of the dusty disc of M 51b at 2 kpc radius. For the combined M 51 system, we find that on average, 5.8% of the dust emission is attributed to the dust heating by the old stellar population of M 51b, of which 4.8% occurs in the M 51a subsystem; 23% of the dust heating is supplied by the old stellar population of M 51a, while the remaining 71.2% arises from the heating by the young stellar populations. Of the 71.2%, 67.8% comes from the yni stellar population, being the main heating agent, and 3.4% comes from the yi stellar population.

In order to have a fair comparison between our results and those by De Looze et al. (2014), we isolate the disc of M 51a

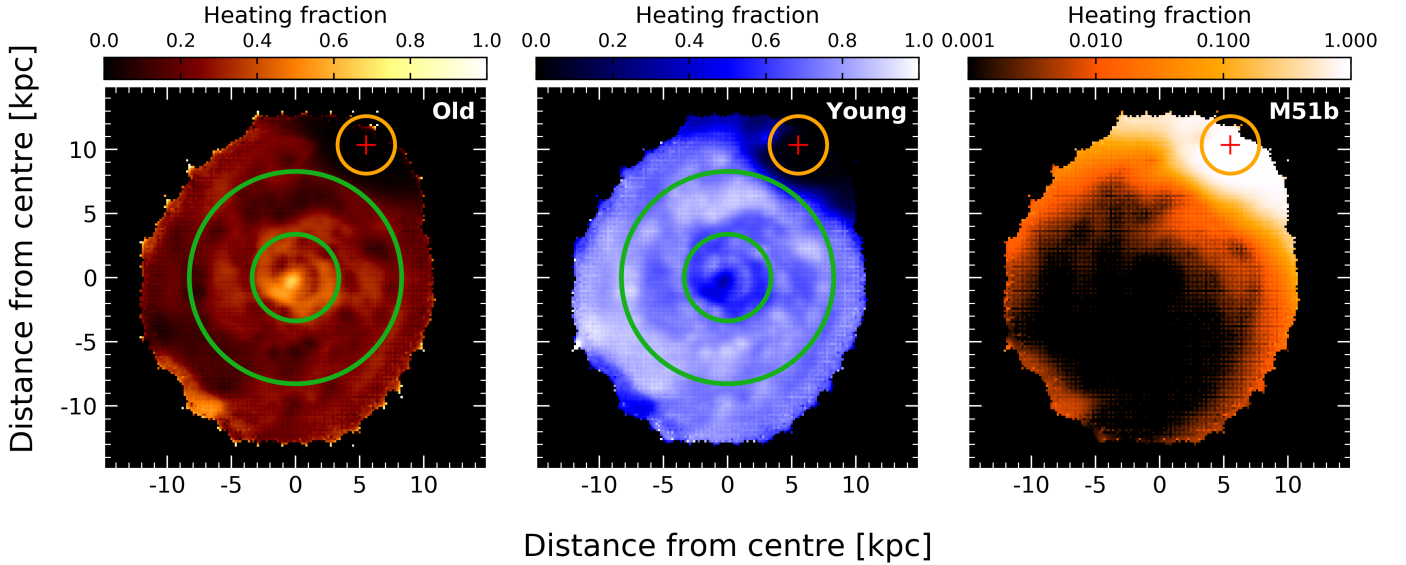


Fig. 6. Dust heating maps of a face-on view of M51, as obtained from the 3D dust cell data. *Left panel:* dust heating fraction by the old stellar population; *middle panel:* dust heating fraction by the young stellar populations; and *right panel:* dust heating fraction by M51b. The rightmost map is shown on a log-scale, and the others are on a linear scale. The inner and outer green circles indicate the 3 kpc and 8 kpc radii, respectively. The red cross is the centre of M51b. The gold circle indicates the extent of the dusty disc of M51b at 2 kpc radius. All maps share the same pixel scale as the PACS 160 μm image: $4.0''$.

and measure the respective heating fractions in a radius of 10 kpc from its centre. Thus, for M51a we find a f_{young} of 72.1% and f_{old} of 23.1%. These values are approximately 9% higher and 14% lower, respectively, than the values reported by De Looze et al. (2014). This difference can be linked to the FUV luminosity that is used to constrain the emission by the young stellar populations, and to the use of different extinction laws related to the corresponding, employed dust models. In the model of De Looze et al. (2014), the FUV emission is underestimated by approximately 18% (see the residual distribution of the FUV map in their Fig. 5). Since we selected our best-fitting model based on a local χ^2 metric, the spatial distribution of the FUV emission in M51a is more accurately reproduced, and thus it provides a more precise measurement of the young heating fraction in the disc.

Inspecting the spatial variation of the young heating fractions in M51a (middle panel of Fig. 6), we see that for the most part the young stellar populations are mostly located in the spiral arms (regions in white), and less in the inter-arm and central areas of the disc (regions in darker blue). On the other hand, paying closer attention to the old heating map (left panel of Fig. 6), we note that the old stellar population dominates the radiation field at the very centre of the galaxy (below 0.5 kpc) with f_{old} up to 68%. However, we measure that the contribution of the young stellar population quickly rises to 57% in the first kpc from the centre, and about 64% in the inner 3 kpc radius. After a distance of 3 kpc, f_{young} remains roughly constant, approximately 76% within a radius of 8 kpc (see also Fig. 9 for the radial profiles of the heating fractions).

The rightmost panel of Fig. 6 shows the extent of the radiation field of M51b. Most of the radiation that comes from the companion galaxy heats up the dust in the upper regions of M51a, donating up to 38% to that purpose. In addition, it is evident that photons can travel deep into the interstellar medium of M51a, even making their way to the far side of the disc. However, it is easier for the photons to propagate in the less dense outskirts of M51a's disc through scattering than to pass through

the more dense areas within the disc. Although f_{M51b} remains under the percentage level around the outskirts of M51a, this could partially explain the increased dust emission at the longest wavelengths that we discussed in Sect. 4.2. As for M51b itself, it contains very little dust, all concentrated in the central region of the galaxy and within a 2 kpc radius (gold circle). The dust, for the most part, is heated by the extremely strong native stellar radiation field, up to 98%. The remaining 2% is evenly contributed by the young and the old stellar populations of M51a. This is no surprise since it is less likely for M51a photons to heat the dust of M51b, firstly because it is harder for photons to escape the dense ISM of M51a, and secondly because of the small extent of the dusty disc of M51b.

Even though the two galaxies are in an early stage of their merging episode, and without any notable signs of their recent encounter, our findings show how the companion galaxy in a major merging system, such as M51, could have a considerable effect on the energy budget of the main galaxy. It is also fair to assume that this effect could only be amplified in minor and major post-mergers. This could significantly impact the derived star formation rates and ISM masses for such systems. Further investigation and quantification of the energy exchange between interacting pairs of different merging stages, through radiative transfer techniques, can be performed on cosmological simulations, like EAGLE (Schaye et al. 2015) or IllustrisTNG (Nelson et al. 2019; Pillepich et al. 2019).

5.2. Implications of the relative distance separation

In this section we discuss how our choice to place M51a and M51b at the same distance may have affected the results that we obtain for the dust heating. In particular, the influence of the radiation field of M51b on M51a. By placing both galaxies in the same plane (centre-to-centre distance separation of ~ 10 kpc), the contribution of heating by M51b is maximised. As mentioned in Sect. 1, M51b can be located at a distance somewhere between 20 kpc (Salo & Laurikainen 2000) and 50 kpc

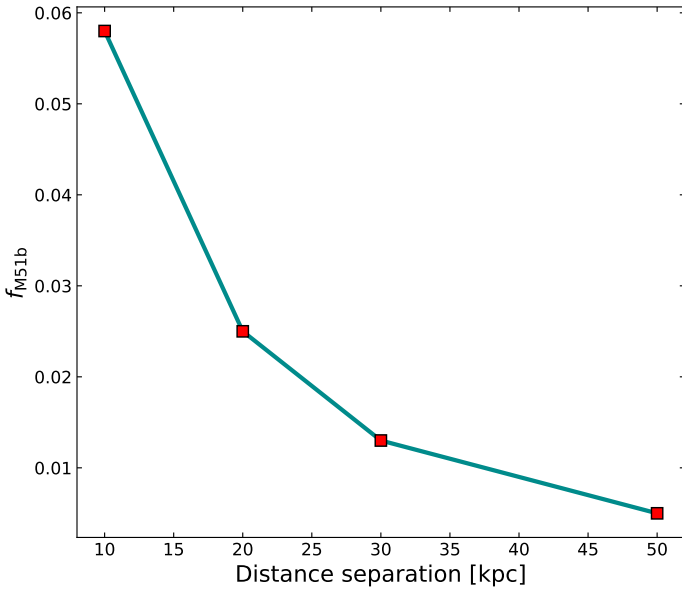


Fig. 7. Global dust heating fraction by M51b against relative distance separation from the centre of M51a.

(Toomre & Toomre 1972) beyond the disc of M51a. Although we tend to lean towards the most up-to-date reported distance (20 kpc), here we investigate three different relative distances between the two galaxies: 20 kpc, 30 kpc, and 50 kpc. In order to measure the global f_{M51b} at these distances, we ran three additional radiative transfer simulations containing just the contribution of M51b and the dust distribution. The IRAC 3.6 μm luminosity of M51b was kept fixed in all three cases ($1.48 \times 10^9 L_\odot$).

Figure 7 shows the global dust heating fraction provided by M51b to the system as a function of the relative distance separation between the two galaxies. As expected, the heating fraction f_{M51b} decreases with distance. Still, the dust heating by M51b remains significant at a relative distance of 20 kpc, with $f_{M51b} = 2.5\%$. In fact, f_{M51b} is even higher for the cells in the inter-arm regions because they are more exposed to M51b now. At a distance of 30 kpc f_{M51b} drops to 1.3%, and remains below the percentage level at 50 kpc distance. It is important to note here that the space between M51a and M51b is not empty, but is filled with tidal debris from their recent interaction (e.g. Watkins et al. 2015) and with hot gas that constitutes the intergalactic medium (IGM). The effect of the IGM on the radiation of M51b is not accounted for in our simulations since there is not yet an implementation for it in SKIRT. So, even if we have modelled these galaxies at their correct distances, it would have been hard to account for the IGM and its effect on the radiation.

5.3. Maps of physical properties

In Fig. 8 we present a set of the most relevant physical maps for a face-on view of M51, as approximated by our radiative transfer model. The information of each physical quantity depicted here was obtained from the 3D dust cells, and projected along the line of sight. The top row shows the physical maps of SFR, stellar mass (M_{star}), and specific star formation rate ($\text{sSFR} = \text{SFR}/M_{\text{star}}$). The combined stellar mass of the two galaxies was estimated through the 3.6 μm luminosities, following the prescriptions of Oliver et al. (2010). The morphological type of each galaxy was taken into account when calculating the M_{star} . We convert the intrinsic FUV luminosity into SFR based on the recipe of Kennicutt & Evans (2012) for a Chabrier (2003)

IMF. The bottom row of Fig. 8 presents the dust temperature (T_{dust}), dust mass (M_{dust}), and dust density (ρ_{dust}) maps. The diffuse dust temperature of each dust cell in our simulations was approximated through the strength of the ISRF (U), following the method used in Nersesian et al. (2020). Assuming that dust is heated by an ISRF with a Milky Way-like spectrum (Mathis et al. 1983) the dust temperatures of the diffuse dust can be approximated as

$$T_{\text{dust}} = T_0 U^{1/(4+\beta)} \quad (5)$$

(Aniano et al. 2012; Nersesian et al. 2019), where T_0 is defined as 18.3 K, the dust temperature is measured in the solar neighbourhood, and $\beta = 1.79$ is the dust emissivity index for the THEMIS dust model.

The top left panel in Fig. 8 shows the distribution of SFR per pixel across M51. Both the spiral arms and the central region of M51a are more pronounced, highlighting the areas where new stars are brewing. Interestingly, we do not find an extremely enhanced SFR in the upper body of M51a. This result is in line with theory that suggests the recent interaction between the two galaxies, 50 to 100 Myr ago, not leading up to a major ongoing starburst. The ability of M51a to produce stars was unaffected by that interaction with M51b, and any signs of star formation are attributed to its normal activity. As a repercussion of the overestimated FUV luminosity in M51b (Sect. 4.2), its nucleus is visible on this particular map, giving a false impression of the actual star formation activity of the galaxy. Despite the overestimation of the SFR in M51b, we are confident that it will not affect the results of this study as we only consider an old stellar population for M51b.

Comparing the SFR to the dust temperature map (or the strength of the ISRF), we find some common features; for example, the central regions of both galaxies as well as the spiral arms are more prominent here. We measure a weighted average of the global dust temperature for the entire system of 16.1 ± 2.2 K, whereas the corresponding dust temperature for M51a is 16.1 ± 1.6 K, and for M51b is 16.8 ± 1.6 K. In the central bulge region of the two galaxies, we measure an average dust temperature of 20.2 ± 1.2 K and 19.6 ± 1.3 K, respectively. The dust temperature in the spiral arms of M51a is at the same level as the dust temperature in the centre, pinpointing the sites of star formation. The inter-arm regions have a moderate dust temperature with typical values ranging from 13 K to 17 K, while the dust temperature takes its lowest values (~ 10 K) around the outer radii of the disc, where it is more unlikely for young stars to be formed.

Consistent with the findings of Mentuch Cooper et al. (2012), the dust in the centre of M51b experiences the effect of the dense ISRF, raising the dust temperature to relatively high levels. At first these results might be thought of as contradictory, due to the apparent correlation between the dust temperature and the star-forming activity of a galaxy. However, several studies have shown that early-type galaxies (galaxies with their ISRF dominated by an evolved stellar population) such as M51b, tend to have warmer dust temperatures than late-type galaxies (e.g. Skibba et al. 2011; Bendo et al. 2012; Boselli et al. 2012; Smith et al. 2012; Viaene et al. 2017; Nersesian et al. 2019). Mentuch Cooper et al. (2012) proposed an AGN as an alternative heating mechanism of the dust in M51b. This assumption was based on the optical signature of AGN reported by Moustakas et al. (2010). Nevertheless, recent centimetre and millimetre continuum observations in the nucleus of M51b do not show evidence of buried AGN activity (Alatalo et al. 2016). On the contrary,

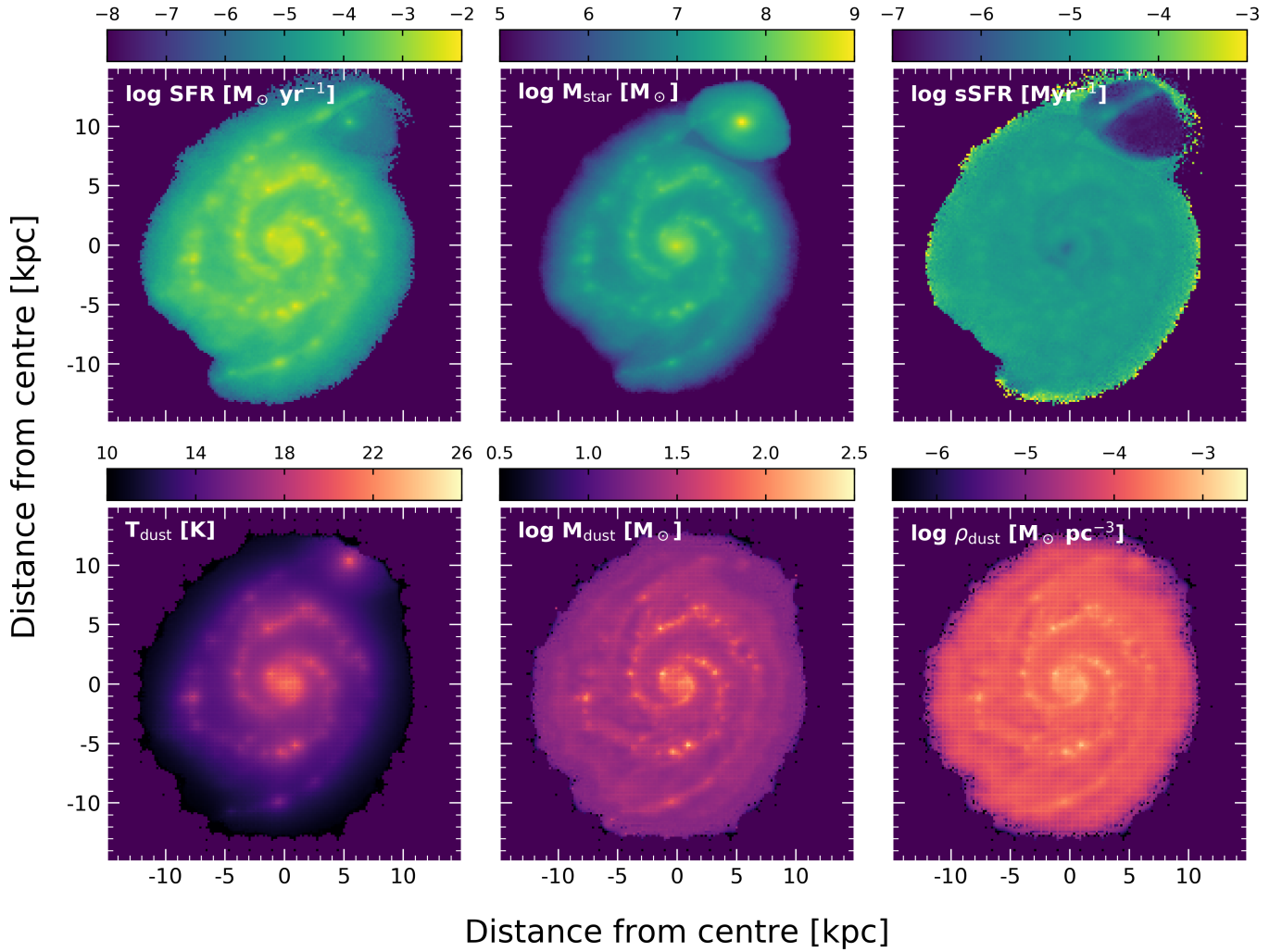


Fig. 8. Various physical maps of a face-on view of M51. *Top row, from left to right:* SFR, stellar mass, and specific star formation rate spatial maps. *Bottom row, from left to right:* dust temperature, dust mass, and dust density spatial maps. All maps, except the dust temperature map, are in log-scale. All maps share the same pixel scale as the PACS $160 \mu\text{m}$ image: $4.0''$.

more evidence has surfaced that support an evolved stellar population as the main dust heating source in M51b (e.g. Alatalo et al. 2016; Eufrasio et al. 2017; Wei et al. 2020).

Another potential dust heating mechanism is collisional heating with electrons in a hot gas. X-ray images from *Chandra* revealed weak X-ray emission in the nucleus of M51b, and two X-ray arcs of cooling gas near the nucleus, most likely produced by feedback from the central supermassive black hole (Schlegel et al. 2016). Schlegel et al. (2016) measured the gas temperature of the nucleus to be 0.61 keV, and that of the two arcs ~ 0.4 and 0.65 keV. The authors also showed the presence of an $\text{H}\alpha$ structure right beyond the X-ray arcs, suggesting that the expanding plasma pushed enough material outward, which could trigger the process of star formation. Finally, UV emission originating from M51a may be an alternative heating source. But as we show in the previous section, the contribution provided by M51a comes down to the percentage level. In reality, the combined effect of the discussed heating mechanisms could explain the increased dust temperature at the very centre of M51b. Notwithstanding, our analysis shows that M51b's native old stellar population is the main dust heating source.

Looking now at the stellar and dust mass maps, we see a smooth distribution for the former and a more structured

distribution for the latter. For M51a there are some features highlighting the spiral structure in the M_{star} map, but they are not as pronounced as in the SFR, T_{dust} , or M_{dust} maps. Similarly, the sSFR map shows even smoother distribution without any sign of structure in the disc, indicating a somewhat constant sSFR throughout the discs of M51a ($2.36 \times 10^{-5} \text{ Myr}^{-1}$), and M51b ($2.70 \times 10^{-7} \text{ Myr}^{-1}$). The sSFR can be considered a measure of the current over the past SFR for a galaxy. The bulge region of M51a has bluer colours indicating that nearly no star formation is happening in the very centre of the galaxy, while the disc of M51b is completely absent supporting the findings of other studies of a complete lack of recent SFR in M51b. On the other hand, the dust density map highlights the fine structure of the spiral arms of M51a. The dust density of M51a peaks at around $3.26 \pm 0.02 \times 10^{-4} M_{\odot} \text{ pc}^{-3}$ in the first 2 kpc radius, and then slightly decreases along the spiral arms. Around the edges and in the inter-arms regions we see a drop in dust density of about an order of magnitude, which further confirms our suspicion of why the photons from M51b were able to propagate so deep in the disc of M51a (see right panel of Fig. 6). As expected, the sites of higher dust density match the regions of enhanced SFR, dust temperature, and stellar mass. Finally, for M51b we measure an average dust density of $8.45 \pm 0.07 \times 10^{-5} M_{\odot} \text{ pc}^{-3}$

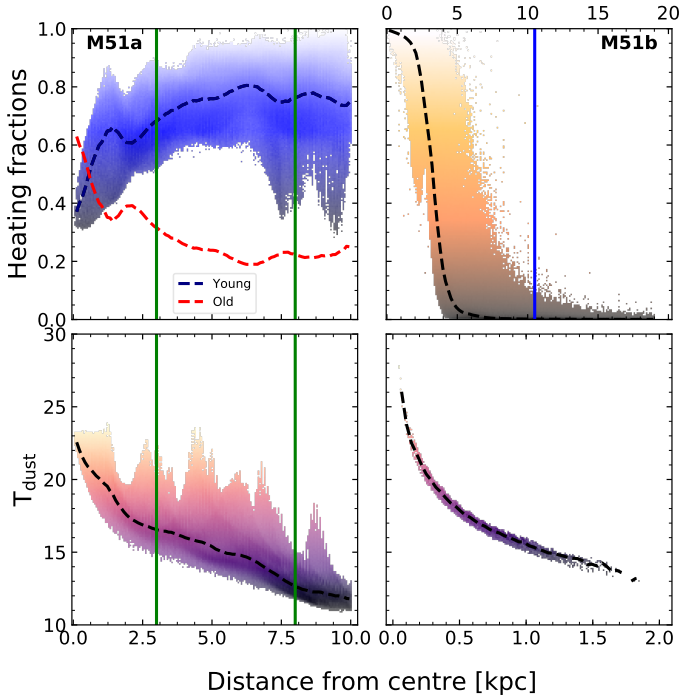


Fig. 9. Various radial profiles of M51 obtained from the 3D dust cell data. *First column, from top to bottom:* radial profiles of the dust heating fractions and the dust temperature for M51a. The vertical green lines indicate the 3 kpc and 8 kpc radii. *Second column, top:* radial profile of f_{M51b} up to 20 kpc radii from the centre of M51b; the blue line gives the location of the central region of M51a. *Second column, bottom:* radial profile of the dust temperature of M51b up to a radius of 2 kpc radii; the dashed lines passing through the points represent the running median. The points are colour-coded according to the same quantity as in the y-axis. The level of transparency indicates the point density.

within a 2 kpc radius. This value is an order of magnitude lower than that measured for the centre of M51a, but it is comparable to the values measured for the dust density in the tidal bridge and outer spiral arms of M51a.

5.4. Radial profiles

Figure 9 shows the radial profiles of various physical quantities as a function of the galactocentric distance from M51a (first column) and from M51b (second column). The dashed lines passing through the data points are the running medians, and show the general trend of the various radial profiles. The top row shows the heating fractions by the different stellar components in our model (see also Eq. (4)). Specifically, the top panel of the first column shows the radial profiles of the heating fractions by the young (blue points and blue dashed line) and old (red dashed line) stellar populations in M51a. Here we see that the central region (up to 1 kpc distance) is populated by a considerable fraction of old stars donating, on average, 43.2% of their energy to the dust heating. Young stars dominate the radiation field of M51a and are the predominant dust heating source in the galactic disc, with a global percentage of 72.1%. Following the running median, we see that the dust heating by the young (old) stellar population sharply rises (falls) within the 1 kpc, then drops (rises) to a local minimum (maximum), and then beyond the 3 kpc radius it stays roughly constant at $\sim 76\%$ in the outer radii.

The top panel of the second column of Fig. 9 shows the extent of the radiative effect that M51b has on the dusty disc of

M51a. The x-axis is the galactocentric distance from M51b up to 20 kpc radius. Within the first few kpcs, the contribution of the stellar radiation of M51b to the energy distribution of M51a is non-negligible. On the contrary, it is responsible for 38% of the dust heating in the area between 2 kpc and 5 kpc from the centre of M51b, which falls right where the upper spiral arms of M51a are located. After the 5 kpc mark, the dust heating provided by M51b drops to a mere 4.5%, while after a distance of 8 kpc it remains below the percentage level. This is a surprising result that could have significant consequences on studies of the ISM properties in pre-mergers where the primary galaxy is often in focus, while the companion considered to have no relevant effect whatsoever. Here we prove that the companion galaxy, even in an early merging phase, as is M51, could significantly alter the energy budget of the main galaxy, and therefore cause erroneous results if not accounted for.

The last row of Fig. 9 showcases the dust temperature of the diffuse dust in each galaxy versus the galactocentric distance. For M51a, we observe a high dust temperature in the centre up to 23.8 K, which slowly drops toward the outer regions. Several peaks of higher dust temperatures can be seen along the radii that indicate the location of the star-forming regions across the spiral arms (see the T_{dust} map in Fig. 8). The outer regions and edges of the disc are occupied by the coldest diffuse dust in the galaxy, with average temperatures of 12.4 ± 0.8 K. On the other hand, M51b shows a smooth dust distribution with the highest temperature in the very centre being 27.7 K, ~ 4 K higher than the dust temperature measured in the centre of M51a. Similarly, [Mentuch Cooper et al. \(2012\)](#) measured a peak in dust temperature of 30 K from single modified blackbody fits to the 70–500 μm images of M51b. As a result of the extremely dense ISRF in the bulge region of M51b, dust can be warmed to such extremely high temperatures. Similarly, when investigating the dust heating in the bulge of the Andromeda galaxy it was found that the old stellar population is responsible for the highest dust temperatures in the galaxy ([Groves et al. 2012](#); [Viaene et al. 2014](#)). Beyond the nucleus, the dust temperature of M51b rapidly drops down to 16.6 ± 0.8 K in the first kpc, while for the next kpc it remains roughly constant with an average dust temperature of 15.0 ± 0.6 K. The trend in the dust temperature is another indication that the diffuse dust density decreases as we move further away from the highly dense nucleus.

6. Discussion

The investigation of UV-to-optical colour-magnitude diagrams (e.g. NUV- r versus M_r) of galaxies revealed that they can be separated into two distinct populations: the “red sequence”, occupied by passive galaxies with red colours, and the “blue cloud”, populated by actively star-forming galaxies of blue colours (e.g. [Wyder et al. 2007](#); [Salim et al. 2007](#), and references therein). This bimodality in the UV-optical colours does appear to be linked with morphology as well. Blue galaxies tend to have a prominent disc structure, while red galaxies tend to be more massive and to exhibit a smooth ellipsoidal shape without signs of a disc or spiral arms ([Gadotti 2009](#); [Wuyts et al. 2011](#); [Whitaker et al. 2015](#)). Further analysis on the global properties of galaxies confirmed the existence of a main sequence (MS) of star-forming galaxies in the $\text{SFR}-M_{\text{star}}$ plane, as well as a region occupied by passive galaxies ([Noeske et al. 2007](#); [Elbaz et al. 2007](#); [Daddi et al. 2007](#)). Inevitably, someone would wonder if such a dichotomy arises from the internal processes that govern the global properties of galaxies. Spatial studies in HII regions of nearby galaxies (e.g. [Rosales-Ortega et al. 2012](#); [Sánchez et al. 2013](#))

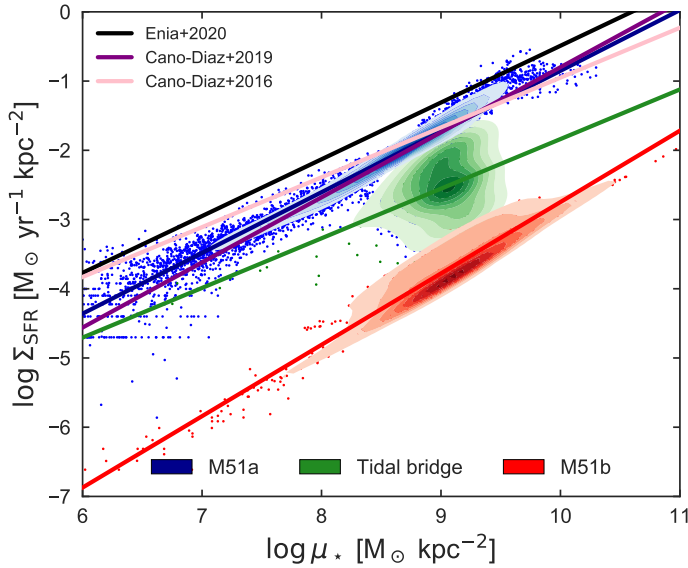


Fig. 10. Σ_{SFR} against stellar mass density for M51 (physical scale of 153.4 pc). The blue density distribution represents the pixels that belong to M51a, the green distribution corresponds to the pixels of the tidal bridge, and the red distribution denotes the pixels of M51b within a 2 kpc radius. The black line is the relation presented in Enia et al. (2020), the purple line is the best-fitting relation from MaNGA (Cano-Díaz et al. 2019), and the pink line is for galaxies in the CALIFA survey (Cano-Díaz et al. 2016). The remaining coloured lines are a fit through the distribution of the same colour.

and in multi-wavelength broadband imaging (e.g. Wuyts et al. 2013; Enia et al. 2020; Morselli et al. 2020) show that the relation between the stellar mass and SFR surface densities holds up on kpc and sub-kpc scales. In this section, we analyse the spatially resolved distributions of μ_* and Σ_{SFR} as encrypted within the pixels of the corresponding maps in Fig. 8. M51 is the ideal system for exploring the $\Sigma_{\text{SFR}}-\mu_*$ plane because M51a is a late-type galaxy of moderate SFR, whereas M51b is more of a “red and dead” galaxy where the SFR activity has ceased altogether. The correlation between f_{young} and sSFR is discussed as well.

6.1. $\Sigma_{\text{SFR}}-\mu_*$ relation for M51

In Fig. 10 we plot Σ_{SFR} against the stellar mass density μ_* , on a physical scale of 153.4 pc. The blue and red KDE distributions belong to all pixels related to M51a, and to M51b within a 2 kpc radius from its centre, respectively. The green distribution depicts the relation for the tidal bridge⁹ that connects the two galaxies. A linear fit for each distribution was performed yielding the following relations,

$$\begin{aligned} \log(\Sigma_{\text{SFR}}/M_{\odot} \text{ yr}^{-1} \text{ kpc}^{-2}) &= 0.88 \log(\mu_*/M_{\odot} \text{ kpc}^{-2}) - 9.64 \text{ [M51a]} \\ \log(\Sigma_{\text{SFR}}/M_{\odot} \text{ yr}^{-1} \text{ kpc}^{-2}) &= 0.72 \log(\mu_*/M_{\odot} \text{ kpc}^{-2}) - 9.01 \text{ [TB]} \\ \log(\Sigma_{\text{SFR}}/M_{\odot} \text{ yr}^{-1} \text{ kpc}^{-2}) &= 1.03 \log(\mu_*/M_{\odot} \text{ kpc}^{-2}) - 12.88 \text{ [M51b]}. \end{aligned} \quad (6)$$

As a reference, we overplot the spatially resolved MS derived by Enia et al. (2020, black line) for eight DustPedia spiral galaxies (including M51a), on spatial scales of 8'' or 0.2–0.8 kpc depending on the distance of each galaxy. They obtained $\log(\Sigma_{\text{SFR}}) = 0.82 \log(\mu_*) - 8.69$. Furthermore, we show the relation fitted by Cano-Díaz et al. (2019, purple line) to ~2000 galaxies from the MaNGA MPL-5 survey (Bundy et al. 2015), on spatial scales of

⁹ The region of the tidal bridge is defined as in Lee et al. (2012).

~1.0 kpc and in the redshift range $0.01 < z < 0.15$. This line has a slope of 0.94. Finally, Cano-Díaz et al. (2016) retrieved a slope of 0.72 (pink line) for a sample of 306 galaxies from the CALIFA survey (Sánchez et al. 2012), at $0.005 < z < 0.03$, and on spatial scales of 0.5–1.5 kpc. All relations have been converted to a Chabrier (2003) IMF.

Several studies of nearby galaxies have worked on a kpc scale or slightly lower, in order to address whether the Σ_{SFR} -to-gas surface density relation holds on sub-galactic scales (e.g. Bigiel et al. 2008; Leroy et al. 2008, 2012; Casasola et al. 2015). In an effort to study how small-scale ISM structure relates to the ability of gas to form stars in M51a, Leroy et al. (2017) used a spatial scale of 370 pc to avoid evolutionary effects of individual regions, and found fluctuations between 370 pc and 1.1 kpc scales. Onodera et al. (2010) found a large dispersion in the Σ_{SFR} inside M33 at a resolution of 80 pc, which they attribute to various evolutionary stages of the giant molecular clouds. Recipes based on energy budget have even been more challenging at sub-kpc scales. Williams et al. (2019) showed that the local dust-energy balance does not hold below scales of 1.5 kpc, while Boquien et al. (2015) showed that below 1.0 kpc hybrid SFR estimators (also based on an energy budget) are not all consistent. In our model we use a spatial scale of ~153 pc similar to the characteristic size of a large HII region (e.g. Rousseau-Nepton et al. 2018), which may challenge the definition of an SFR calibration. Consequently, we tested the consistency of the MS of M51 on different spatial scales. Instead of running new simulations with lower resolution, we regrid the output to two additional scales of 460 pc and 1500 pc, and then apply the SFR and M_{star} recipes to the data. The fitted slopes of M51a and M51b remain roughly the same across the different spatial scales. For M51a we retrieve a slope of 0.92 and 0.89, while for M51b we obtain a slope of 0.92 and 1.07, for the respective scales. All three representations of the MS of M51 have similar slopes, despite the change in the physical scales, which makes us confident that the used recipes can be applied on scales at least up to 150 pc.

For M51a the total dispersion of MS is $\sigma = 0.10$, for M51b $\sigma = 0.23$, and for the tidal bridge $\sigma = 0.15$. The scatter of M51a is marginally consistent with the typical range of 0.13–0.35 reported in previous studies on the spatially resolved MS (Magdis et al. 2016; Maragkoudakis et al. 2017; Hsieh et al. 2017; Hall et al. 2018; Enia et al. 2020). We also investigate whether the scatter of the MS varies with mass by splitting the data in three mass bins: $6 \leq \log \mu_* < 7.5$, $7.5 \leq \log \mu_* < 9$, and $\log \mu_* \geq 9$. For M51a we find a low dispersion in the first two bins of $\sigma \sim 0.07$ and an increased scatter for the highest mass bin of $\sigma = 0.13$. For M51b we find an increasing dispersion with $\log \mu_*$: $\sigma = 0.06$, $\sigma = 0.21$, and $\sigma = 0.24$, respectively for each bin. We do not provide the dispersion per bin for the tidal bridge due to the reduced number of points in the lowest and highest mass bins.

Interestingly enough, the pixel distribution of each galaxy occupies two distinct regions in the $\Sigma_{\text{SFR}}-\mu_*$ plane. Their position in Fig. 10 is purely a consequence of their SFH. The distribution of M51a falls predominately on what is described as the MS of star-forming galaxies. The slope we retrieve for M51a is similar to the MS obtained by Enia et al. (2020), but a vertical shift is evident possibly due to the different methods of estimating the SFR and M_{star} . Although the slopes for the CALIFA and MaNGA surveys differ from that of M51a, all share about the same locus. The steep slope of the observed MS indicates the change in Σ_{SFR} per μ_* in the different regions of M51a, ranging approximately over three orders of magnitude. On the other hand, the distribution related to M51b reside on a well-defined

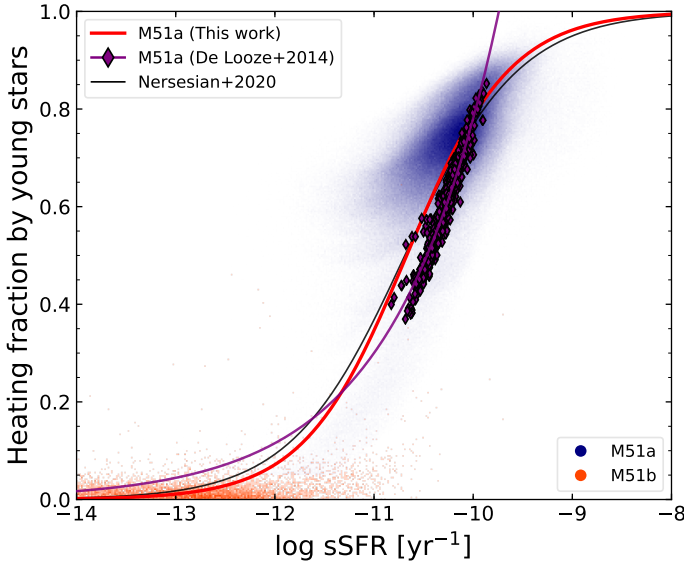


Fig. 11. Relation between sSFR and f_{young} . The blue points represent the dust cells that belong to M51a within a 10 kpc radius of its centre, and the orange points the dust cells of M51b. The level of transparency indicates the points density. The red line is the fit through the points of M51a with Eq. (7). The purple diamonds are the pixel values of M51a, and the purple line is the power-law fit to that data from the model of De Looze et al. (2014). The black line shows the MS of galaxies as derived in Nersesian et al. (2020) by fitting the voxels of the radiative transfer models of six face-on late-type galaxies.

sequence, but with lower values (2–3 orders of magnitude) of Σ_{SFR} than that of M51a. The red sequence has a steeper slope, with Σ_{SFR} varying about five orders of magnitude. The tidal bridge seems to have a well-defined star-forming locus in the plane of Fig. 10, possibly as a result of the tidal interaction. The stellar bridge not only connects the two galaxies in physical space, but also along the $\Sigma_{\text{SFR}}-\mu_{\star}$ relation. For a fixed μ_{\star} , the Σ_{SFR} of the tidal bridge is always lower than the Σ_{SFR} of M51a, and higher than the Σ_{SFR} of M51b. This indicates that the SFR in that region was once enhanced during the passage of M51b, through the exchange of gas between the two components, enriching one of them and depleting the other, and that it is now going towards a quenching phase. However, as stated in Lee et al. (2012), it is still unclear whether the young stars populating the bridge were born in situ or if they migrated from the spiral arm of M51a.

6.2. Correlation between young heating fraction and sSFR

Another tight correlation that reveals the spatial variation of star formation is the one between the young heating fraction and the sSFR (De Looze et al. 2014; Viaene et al. 2016, 2017; Verstocken et al. 2020; Nersesian et al. 2019, 2020). In Nersesian et al. (2020), the authors extended the parameter range of the relation (first presented by De Looze et al. 2014, for M51a) by concentrating the results from the radiation transfer models of six late-type face-on spiral galaxies, and derived a sequence for sub-kpc regions within those galaxies. Figure 11 depicts the young heating fraction against the sSFR of M51a (blue points), and extends the parameter space of the relation by including the data of a non-star-forming galaxy, M51b (orange points). We also overplot the pixel data values (purple diamonds), as well as the best-fitting power law (purple solid line) from the radiative transfer model of M51a by De Looze et al.

(2014). Finally, Fig. 11 shows the sequence derived by Nersesian et al. (2020) using the following equation:

$$f_{\text{young}} = \frac{1}{2} \left[1 - \tanh \left(a \log \left(\text{sSFR} / \text{yr}^{-1} \right) + b \right) \right]. \quad (7)$$

The same equation is used to fit the relation for M51a (red line). The fitting yields $a = -0.96$ and $b = -10.30$. Comparing the data from the two different radiative transfer models of M51a, it is evident that they are in very good agreement, residing within the same parameter space, but with a slight offset towards lower sSFR for our model. This small offset is attributed to the different SFR recipes used by the two studies. Overall, the main group of data points of M51a reside in the middle region of the solid black line, while the orange cloud of points related to M51b is located at the lower left end of the same relation. In contrast to Fig. 10, where the data from both galaxies were separated into two distinct regions, here we see that there is a continuous change in the properties (and in morphology) of the two galaxies along the sequence.

7. Summary and conclusions

We have constructed a detailed 3D radiative transfer model for the interacting system M51, using the state-of-the-art Monte Carlo code SKIRT. The scope of this study was to investigate the dust-heating processes in a merging system, and to assess the radiative influence of the companion, on the energy budget of its parent galaxy. As a continuation of this series of papers, which started with the study of M51a (De Looze et al. 2014), we also presented an updated model of the grand design spiral galaxy M51a based on the methodology presented in Verstocken et al. (2020). Our model has been validated by comparing the simulated SEDs with the observational data across the entire UV to submm wavelength range, yielding a best-fitting description of the interacting system. Here we list our main findings:

- 40.7% of the bolometric luminosity is absorbed by dust in M51. This fraction is in line with the mean values determined by Bianchi et al. (2018) for late-type spiral galaxies of morphological type Sb-Sc.
- While the young stellar population is the main dust heating agent of M51, the older stellar population also has quite an active role in the process of dust heating. The global f_{young} (f_{old}) fraction of M51 is 71.2% (23%), while the remaining 5.8% is provided by M51b. By isolating each galaxy, we measure that M51a's diffuse dust is heated by a f_{young} (f_{old}) of 72.1% (23.1%) and a f_{M51b} of 4.8%. The respective heating fractions for M51b's dust are $f_{\text{young}} + f_{\text{old}} = 2\%$, and a f_{M51b} of 98%.
- We find that the extent of the contribution of the dust heating by the companion galaxy depends on the density of the ISM, with photons easily propagating to the less dense outskirts of M51a's disc through scattering, while they are absorbed by the denser regions in the upper body of M51a. Specifically, the contribution of the radiation field of M51b is significant up to a distance of 5 kpc from its centre, with a heating fraction of $\sim 38\%$. After the 5 kpc mark the significance of this heating agent drops below 10% and remains under the percentage level beyond a radius of 8 kpc.
- On average, the diffuse dust temperature at the central region of both galaxies is warmer than the dust temperatures found at their discs, with T_{dust} decreasing with galactocentric distance. The young stellar population is responsible for the warmer T_{dust} in the spiral arms and near the star-forming dust clouds of M51a, whereas the dense old ISRF in the

nucleus of M 51b, raises the dust temperature to relatively high levels. The weighted average dust temperature of M 51a is 16.1 ± 1.6 K and of M 51b is 16.8 ± 1.8 K.

- We further confirm that the pixel distribution related to each galaxy falls into two distinct regions in the $\Sigma_{\text{SFR}}-\mu_{\star}$ plane (physical scale of 153.4 pc). The data from M 51a are located in the region of the diagram that resembles the MS of star-forming galaxies, while the data from M 51b occupy the parameter space known as the red sequence of non-star-forming galaxies.
- Exploring the $f_{\text{young}}-\text{sSFR}$ plane (De Looze et al. 2014; Nersesian et al. 2020), we find that instead of two distinct galaxy populations, galaxies follow a continuous relation depending on their intrinsic properties and morphology.

Our results, model configuration (ski file), and model input data (component maps) are publicly available on the DustPedia archive¹⁰ under the SKIRT tab, so that anyone can reproduce our work.

Acknowledgements. We would like to thank the anonymous referee for providing detailed comments and suggestions, which helped to improve the presentation of the manuscript. AN, EMX, gratefully acknowledges the support by Greece and the European Union (European Social Fund-ESF) through the Operational Programme “Human Resources Development, Education and Lifelong Learning 2014–2020” in the context of the project “Anatomy of galaxies: their stellar and dust content through cosmic time” (MIS 5052455). DustPedia is a collaborative focused research project supported by the European Union under the Seventh Framework Programme (2007–2013) call (proposal no. 606847). The participating institutions are: Cardiff University, UK; National Observatory of Athens, Greece; Ghent University, Belgium; Université Paris Sud, France; National Institute for Astrophysics, Italy and CEA, France. The computational resources (Stevin Supercomputer Infrastructure) and services used in this work were provided by the VSC (Flemish Supercomputer Center), funded by Ghent University, FWO and the Flemish Government – department EWI. This research made use of Astropy (<http://www.astropy.org>), a community-developed core Python package for Astronomy (Astropy Collaboration 2013, 2018). This research has made use of the NASA/IPAC Infrared Science Archive (IRSA; <http://irsa.ipac.caltech.edu>), and the NASA/IPAC Extragalactic Database (NED; <https://ned.ipac.caltech.edu>), both of which are operated by the Jet Propulsion Laboratory, California Institute of Technology, under contract with the National Aeronautics and Space Administration.

References

- Alatalo, K., Aladro, R., Nyland, K., et al. 2016, *ApJ*, **830**, 137
- Aniano, G., Draine, B. T., Calzetti, D., et al. 2012, *ApJ*, **756**, 138
- Astropy Collaboration (Robitaille, T. P., et al.) 2013, *A&A*, **558**, A33
- Astropy Collaboration (Price-Whelan, A. M., et al.) 2018, *AJ*, **156**, 123
- Baes, M. 2020, in *IAU Symposium*, eds. M. Boquien, E. Lusso, C. Gruppioni, & P. Tissera, 341, 26
- Baes, M., & Camps, P. 2015, *Astron. Comput.*, **12**, 33
- Baes, M., Verstaappen, J., De Looze, I., et al. 2011, *ApJS*, **196**, 22
- Barnes, J. E., & Hernquist, L. 1992, *ARA&A*, **30**, 705
- Barnes, J. E., & Hernquist, L. 1996, *ApJ*, **471**, 115
- Bendo, G. J., Draine, B. T., Engelbracht, C. W., et al. 2008, *MNRAS*, **389**, 629
- Bendo, G. J., Boselli, A., Dariush, A., et al. 2012, *MNRAS*, **419**, 1833
- Bianchi, S., De Vis, P., Viaene, S., et al. 2018, *A&A*, **620**, A112
- Bigiel, F., Leroy, A., Walter, F., et al. 2008, *AJ*, **136**, 2846
- Boquien, M., Calzetti, D., Aalto, S., et al. 2015, *A&A*, **578**, A8
- Boquien, M., Burgarella, D., Roehlly, Y., et al. 2019, *A&A*, **622**, A103
- Boselli, A., Ciesla, L., Cortese, L., et al. 2012, *A&A*, **540**, A54
- Boulade, O., Sauvage, M., Altieri, B., et al. 1996, *A&A*, **315**, L85
- Bradley, L. D., Kaiser, M. E., & Baan, W. A. 2004, *ApJ*, **603**, 463
- Bradley, L., Sipocz, B., Robitaille, T., et al. 2018, <https://doi.org/10.5281/zenodo.1340699>
- Bresolin, F., Garnett, D. R., & Kennicutt, R. C., Jr. 2004, *ApJ*, **615**, 228
- Bruzual, G., & Charlot, S. 2003, *MNRAS*, **344**, 1000
- Bundy, K., Bershady, M. A., Law, D. R., et al. 2015, *ApJ*, **798**, 7
- Calzetti, D., Armus, L., Bohlin, R. C., et al. 2000, *ApJ*, **533**, 682
- Calzetti, D., Kennicutt, R. C., Engelbracht, C. W., et al. 2007, *ApJ*, **666**, 870
- Camps, P., & Baes, M. 2015, *Astron. Comput.*, **9**, 20
- Camps, P., & Baes, M. 2020, *Astron. Comput.*, **31**, 100381
- Camps, P., Baes, M., & Saitly, W. 2013, *A&A*, **560**, A35
- Cano-Díaz, M., Sánchez, S. F., Zibetti, S., et al. 2016, *ApJ*, **821**, L26
- Cano-Díaz, M., Ávila-Reese, V., Sánchez, S. F., et al. 2019, *MNRAS*, **488**, 3929
- Cardelli, J. A., Clayton, G. C., & Mathis, J. S. 1989, *ApJ*, **345**, 245
- Casasola, V., Bettoni, D., & Galletta, G. 2004, *A&A*, **422**, 941
- Casasola, V., Hunt, L., Combes, F., & García-Burillo, S. 2015, *A&A*, **577**, A135
- Chabrier, G. 2003, *PASP*, **115**, 763
- Ciesla, L., Boselli, A., Elbaz, D., et al. 2016, *A&A*, **585**, A43
- Clark, C. J. R., Verstocken, S., Bianchi, S., et al. 2018, *A&A*, **609**, A37
- Clements, D. L., Sutherland, W. J., McMahon, R. G., & Saunders, W. 1996, *MNRAS*, **279**, 477
- Combes, F., Prugniel, P., Rampazzo, R., & Sulentic, J. W. 1994, *A&A*, **281**, 725
- Conroy, C. 2013, *ARA&A*, **51**, 393
- Cortese, L., Boselli, A., Franzetti, P., et al. 2008, *MNRAS*, **386**, 1157
- Cox, T. J., Dutta, S. N., Di Matteo, T., et al. 2006a, *ApJ*, **650**, 791
- Cox, T. J., Jonsson, P., Primack, J. R., & Somerville, R. S. 2006b, *MNRAS*, **373**, 1013
- Cox, T. J., Jonsson, P., Somerville, R. S., Primack, J. R., & Dekel, A. 2008, *MNRAS*, **384**, 386
- Cutri, R. M., Skrutskie, M. F., van Dyk, S., et al. 2003, *VizieR Online Data Catalog: II/2246*
- Daddi, E., Dickinson, M., Morrison, G., et al. 2007, *ApJ*, **670**, 156
- Dasyra, K. M., Tacconi, L. J., Davies, R. I., et al. 2006, *ApJ*, **638**, 745
- Davies, J. I., Baes, M., Bianchi, S., et al. 2017, *PASP*, **129**, 044102
- Decleir, M., De Looze, I., Boquien, M., et al. 2019, *MNRAS*, **486**, 743
- De Geyter, G., Baes, M., Camps, P., et al. 2014, *MNRAS*, **441**, 869
- De Looze, I., Fritz, J., Baes, M., et al. 2014, *A&A*, **571**, A69
- de Vaucouleurs, G., de Vaucouleurs, A., Corwin, H. G., et al. 1995, *VizieR Online Data Catalog: VII/155*
- Di Matteo, P., Combes, F., Melchior, A. L., & Semelin, B. 2007, *A&A*, **468**, 61
- Dobbs, C. L., Theis, C., Pringle, J. E., & Bate, M. R. 2010, *MNRAS*, **403**, 625
- Draine, B. T., & Li, A. 2007, *ApJ*, **657**, 810
- Draine, B. T., Dale, D. A., Bendo, G., et al. 2007, *ApJ*, **663**, 866
- Durrell, P. R., Mihos, J. C., Feldmeier, J. J., Jacoby, G. H., & Ciardullo, R. 2003, *ApJ*, **582**, 170
- Eisenstein, D. J., Weinberg, D. H., Agol, E., et al. 2011, *AJ*, **142**, 72
- Elbaz, D., Daddi, E., Le Borgne, D., et al. 2007, *A&A*, **468**, 33
- Ellison, S. L., Patton, D. R., Simard, L., & McConnell, A. W. 2008, *AJ*, **135**, 1877
- Ellison, S. L., Patton, D. R., Mendel, J. T., & Scudder, J. M. 2011, *MNRAS*, **418**, 2043
- Ellison, S. L., Mendel, J. T., Patton, D. R., & Scudder, J. M. 2013, *MNRAS*, **435**, 3627
- Enia, A., Rodighiero, G., Morselli, L., et al. 2020, *MNRAS*, **493**, 4107
- Eufrazio, R. T., Lehmer, B. D., Zezas, A., et al. 2017, *ApJ*, **851**, 10
- Gadotti, D. A. 2009, *MNRAS*, **393**, 1531
- Galametz, M., Kennicutt, R. C., Calzetti, D., et al. 2013, *MNRAS*, **431**, 1956
- Galliano, F. 2018, *MNRAS*, **476**, 1445
- Galliano, F., Madden, S. C., Tielens, A. G. G. M., Peeters, E., & Jones, A. P. 2008, *ApJ*, **679**, 310
- Galliano, F., Galametz, M., & Jones, A. P. 2018, *ARA&A*, **56**, 673
- Groves, B., Dopita, M. A., Sutherland, R. S., et al. 2008, *ApJS*, **176**, 438
- Groves, B., Krause, O., Sandstrom, K., et al. 2012, *MNRAS*, **426**, 892
- Hall, C., Courteau, S., Jarrett, T., et al. 2018, *ApJ*, **865**, 154
- Hirashita, H., & Kuo, T.-M. 2011, *MNRAS*, **416**, 1340
- Hsieh, B. C., Lin, L., Lin, J. H., et al. 2017, *ApJ*, **851**, L24
- Jones, A. P., Fanciullo, L., Köhler, M., et al. 2013, *A&A*, **558**, A62
- Jones, A. P., Köhler, M., Ysard, N., Bocchio, M., & Verstraete, L. 2017, *A&A*, **602**, A46
- Kauffmann, G., & Haehnelt, M. 2000, *MNRAS*, **311**, 576
- Kauffmann, G., Colberg, J. M., Diaferio, A., & White, S. D. M. 1999a, *MNRAS*, **303**, 188
- Kauffmann, G., Colberg, J. M., Diaferio, A., & White, S. D. M. 1999b, *MNRAS*, **307**, 529
- Kaviraj, S. 2014, *MNRAS*, **440**, 2944
- Kennicutt, R. C., Jr. 1998, *ARA&A*, **36**, 189
- Kennicutt, R. C., & Evans, N. J. 2012, *ARA&A*, **50**, 531
- Kennicutt, R. C., Jr., Armus, L., Bendo, G., et al. 2003, *PASP*, **115**, 928
- Köhler, M., Stepnik, B., Jones, A. P., et al. 2012, *A&A*, **548**, A61
- Köhler, M., Jones, A., & Ysard, N. 2014, *A&A*, **565**, L9
- Köhler, M., Ysard, N., & Jones, A. P. 2015, *A&A*, **579**, A15
- Kohn, K., Tosaki, T., Matsushita, S., et al. 2002, *PASJ*, **54**, 541
- Kroupa, P. 2002, *Science*, **295**, 82
- Lee, J. H., Hwang, N., & Lee, M. G. 2011, *ApJ*, **735**, 75
- Lee, J. H., Kim, S. C., Ree, C. H., et al. 2012, *ApJ*, **754**, 80
- Leitherer, C., Li, I.-H., Calzetti, D., & Heckman, T. M. 2002, *ApJS*, **140**, 303

¹⁰ <http://dustpedia.astro.noa.gr>

- Leroy, A. K., Walter, F., Brinks, E., et al. 2008, *AJ*, **136**, 2782
- Leroy, A. K., Bigiel, F., de Blok, W. J. G., et al. 2012, *AJ*, **144**, 3
- Leroy, A. K., Schinnerer, E., Hughes, A., et al. 2017, *ApJ*, **846**, 71
- Lisenfeld, U., Xu, C. K., Gao, Y., et al. 2019, *A&A*, **627**, A107
- Magdis, G. E., Bureau, M., Stott, J. P., et al. 2016, *MNRAS*, **456**, 4533
- Maragkoudakis, A., Zezas, A., Ashby, M. L. N., & Willner, S. P. 2017, *MNRAS*, **466**, 1192
- Maraston, C. 2005, *MNRAS*, **362**, 799
- Mathis, J. S., Mezger, P. G., & Panagia, N. 1983, *A&A*, **128**, 212
- Mentuch Cooper, E., Wilson, C. D., Foyle, K., et al. 2012, *ApJ*, **755**, 165
- Mihos, J. C., & Hernquist, L. 1996, *ApJ*, **464**, 641
- Moreno, J., Torrey, P., Ellison, S. L., et al. 2019, *MNRAS*, **485**, 1320
- Morrissey, P., Conrow, T., Barlow, T. A., et al. 2007, *ApJS*, **173**, 682
- Morselli, L., Rodighiero, G., Enia, A., et al. 2020, *MNRAS*, **496**, 4606
- Mosenkov, A. V., Baes, M., Bianchi, S., et al. 2019, *A&A*, **622**, A132
- Moustakas, J., Kennicutt, R. C., Jr., Tremonti, C. A., et al. 2010, *ApJS*, **190**, 233
- Naab, T., & Trujillo, I. 2006, *MNRAS*, **369**, 625
- Nelson, D., Pillepich, A., Springel, V., et al. 2019, *MNRAS*, **490**, 3234
- Nersesian, A., Xilouris, E. M., Bianchi, S., et al. 2019, *A&A*, **624**, A80
- Nersesian, A., Verstocken, S., Viaene, S., et al. 2020, *A&A*, **637**, A25
- Noeske, K. G., Weiner, B. J., Faber, S. M., et al. 2007, *ApJ*, **660**, L43
- Noll, S., Burgarella, D., Giovannoli, E., et al. 2009, *A&A*, **507**, 1793
- Oliver, S., Frost, M., Farrah, D., et al. 2010, *MNRAS*, **405**, 2279
- Onodera, S., Kuno, N., Tosaki, T., et al. 2010, *ApJ*, **722**, L127
- Peeters, E., Bauschlicher, C. W., Jr., & Allamandola, L. J. 2017, *ApJ*, **836**, 198
- Pilbratt, G. L., Riedinger, J. R., Passvogel, T., et al. 2010, *A&A*, **518**, L1
- Pillepich, A., Nelson, D., Springel, V., et al. 2019, *MNRAS*, **490**, 3196
- Popescu, C. C., Misiriotis, A., Kylafis, N. D., Tuffs, R. J., & Fischera, J. 2000, *A&A*, **362**, 138
- Rosales-Ortega, F. F., Sánchez, S. F., Iglesias-Páramo, J., et al. 2012, *ApJ*, **756**, L31
- Rousseau-Nepton, L., Robert, C., Martin, R. P., Drissen, L., & Martin, T. 2018, *MNRAS*, **477**, 4152
- Saftly, W., Camps, P., Baes, M., et al. 2013, *A&A*, **554**, A10
- Saftly, W., Baes, M., & Camps, P. 2014, *A&A*, **561**, A77
- Salim, S., Rich, R. M., Charlot, S., et al. 2007, *ApJS*, **173**, 267
- Salo, H., & Laurikainen, E. 2000, *MNRAS*, **319**, 377
- Salo, H., Laurikainen, E., Laine, J., et al. 2015, *ApJS*, **219**, 4
- Salpeter, E. E. 1955, *ApJ*, **121**, 161
- Sánchez, S. F., Kennicutt, R. C., Gil de Paz, A., et al. 2012, *A&A*, **538**, A8
- Sánchez, S. F., Rosales-Ortega, F. F., Jungwiert, B., et al. 2013, *A&A*, **554**, A58
- Sanders, D. B., & Mirabel, I. F. 1996, *ARA&A*, **34**, 749
- Satyapal, S., Sambruna, R. M., & Dudik, R. P. 2004, *A&A*, **414**, 825
- Schaye, J., Crain, R. A., Bower, R. G., et al. 2015, *MNRAS*, **446**, 521
- Schlegel, E. M., Jones, C., Machacek, M., & Vega, L. D. 2016, *ApJ*, **823**, 75
- Sheth, K., Regan, M., Hinz, J. L., et al. 2010, *PASP*, **122**, 1397
- Skibba, R. A., Engelbracht, C. W., Dale, D., et al. 2011, *ApJ*, **738**, 89
- Skrutskie, M. F., Cutri, R. M., Stiening, R., et al. 2006, *AJ*, **131**, 1163
- Smith, M. W. L., Gomez, H. L., Eales, S. A., et al. 2012, *ApJ*, **748**, 123
- Somerville, R. S., & Primack, J. R. 1999, *MNRAS*, **310**, 1087
- Springel, V., White, S. D. M., Jenkins, A., et al. 2005, *Nature*, **435**, 629
- Terashima, Y., & Wilson, A. S. 2001, *ApJ*, **560**, 139
- Theis, C., & Spinneker, C. 2003, *Ap&SS*, **284**, 495
- Thirlwall, J. J., Popescu, C. C., Tuffs, R. J., et al. 2020, *MNRAS*, **495**, 835
- Thronson, H. A., Jr., Rubin, H., & Ksir, A. 1991, *MNRAS*, **252**, 550
- Tikhonov, N. A., Galazutdinova, O. A., & Tikhonov, E. N. 2009, *Astron. Lett.*, **35**, 599
- Toomre, A. 1977, in *Evolution of Galaxies and Stellar Populations*, eds. B. M. Tinsley, D. C. Larson, & R. B. Gehret, 401
- Toomre, A., & Toomre, J. 1972, *ApJ*, **178**, 623
- Verstocken, S., Van De Putte, D., Camps, P., & Baes, M. 2017, *Astron. Comput.*, **20**, 16
- Verstocken, S., Nersesian, A., Baes, M., et al. 2020, *A&A*, **637**, A24
- Viaene, S., Fritz, J., Baes, M., et al. 2014, *A&A*, **567**, A71
- Viaene, S., Baes, M., Bendo, G., et al. 2016, *A&A*, **586**, A13
- Viaene, S., Baes, M., Tamm, A., et al. 2017, *A&A*, **599**, A64
- Viaene, S., Nersesian, A., Fritz, J., et al. 2020, *A&A*, **638**, A150
- Violino, G., Ellison, S. L., Sargent, M., et al. 2018, *MNRAS*, **476**, 2591
- Walcher, J., Groves, B., Budavári, T., & Dale, D. 2011, *Ap&SS*, **331**, 1
- Watkins, A. E., Mihos, J. C., & Harding, P. 2015, *ApJ*, **800**, L3
- Wei, P., Zou, H., Lin, L., et al. 2020, ArXiv e-prints [arXiv:2007.06231]
- Werner, M. W., Roellig, T. L., Low, F. J., et al. 2004, *ApJS*, **154**, 1
- Weston, M. E., McIntosh, D. H., Brodwin, M., et al. 2017, *MNRAS*, **464**, 3882
- Whitaker, K. E., Franx, M., Bezanson, R., et al. 2015, *ApJ*, **811**, L12
- Williams, T. G., Baes, M., De Looze, I., et al. 2019, *MNRAS*, **487**, 2753
- Woods, D. F., & Geller, M. J. 2007, *AJ*, **134**, 527
- Wright, E. L., Eisenhardt, P. R. M., Mainzer, A. K., et al. 2010, *AJ*, **140**, 1868
- Wuyts, S., Förster Schreiber, N. M., van der Wel, A., et al. 2011, *ApJ*, **742**, 96
- Wuyts, S., Förster Schreiber, N. M., Nelson, E. J., et al. 2013, *ApJ*, **779**, 135
- Wyder, T. K., Martin, D. C., Schiminovich, D., et al. 2007, *ApJS*, **173**, 293
- Xilouris, E. M., Byun, Y. I., Kylafis, N. D., Paleologou, E. V., & Papamastorakis, J. 1999, *A&A*, **344**, 868
- York, D. G., Adelman, J., Anderson, J. E., Jr, et al. 2000, *AJ*, **120**, 1579

Appendix A: Global photometry

Table A.1 summarises the final flux densities and their corresponding uncertainties extracted from the global aperture photometry of the different galaxy regions listed in Table 1 and shown in Fig. 1. The global flux densities were fitted with the SED code CIGALE (see Sect. 2.5), and were used to constrain

the radiative transfer model of M 51 (see Sect. 4). Marked in boldface are the bands that were not used in our modelling.

Table A.2 gives an overview of the images that are used to produce the spatial distribution of the various components in our radiative transfer model of M 51, as well as the simulation output maps that are used to derive the local (per pixel) physical parameters.

Table A.1. Integrated flux densities for our galaxy sample in this paper, listed by increasing central wavelength.

Instrument	Band	λ_{eff} [μm]	Pixel scale [arcsec]	NGC 5194 (M 51a)	NGC 5195 (M 51b)	M 51
				Flux density [Jy]	Flux density [Jy]	Flux density [Jy]
GALEX	FUV	0.154	3.2	0.118 ± 0.006	0.002 ± 0.001	0.119 ± 0.006
GALEX	NUV	0.227	3.2	0.194 ± 0.005	0.005 ± 0.001	0.198 ± 0.006
SDSS	<i>u</i>	0.359	0.45	0.488 ± 0.006	0.074 ± 0.001	0.537 ± 0.007
SDSS	<i>g</i>	0.464	0.45	1.354 ± 0.011	0.278 ± 0.002	1.603 ± 0.013
SDSS	<i>r</i>	0.612	0.45	2.160 ± 0.017	0.584 ± 0.005	2.702 ± 0.022
KPNO	H α	0.657	0.3	2.943 ± 0.230	0.470 ± 0.148	3.450 ± 0.023
SDSS	<i>i</i>	0.744	0.45	2.571 ± 0.018	0.876 ± 0.006	3.641 ± 0.025
SDSS	<i>z</i>	0.89	0.45	3.060 ± 0.024	1.110 ± 0.009	4.197 ± 0.034
2MASS	<i>J</i>	1.235	1.0	3.538 ± 0.099	1.659 ± 0.046	5.571 ± 0.156
2MASS	<i>H</i>	1.662	1.0	3.828 ± 0.107	2.050 ± 0.057	5.754 ± 0.161
2MASS	<i>K_s</i>	2.159	1.0	3.446 ± 0.097	1.660 ± 0.046	5.295 ± 0.148
WISE	W1	3.352	1.37	2.368 ± 0.069	0.885 ± 0.026	3.260 ± 0.095
IRAC	I1	3.508	0.75	2.515 ± 0.075	0.879 ± 0.026	3.405 ± 0.102
IRAC	I2	4.437	0.75	1.608 ± 0.048	0.561 ± 0.017	2.286 ± 0.069
WISE	W2	4.603	1.37	1.408 ± 0.048	0.516 ± 0.018	2.076 ± 0.071
IRAC	I3	5.628	0.6	5.146 ± 0.154	0.666 ± 0.020	5.894 ± 0.177
IRAC	I4	7.589	0.6	12.899 ± 0.387	1.037 ± 0.031	14.476 ± 0.434
WISE	W3	11.56	1.37	8.520 ± 0.392	0.851 ± 0.039	9.837 ± 0.452
WISE	W4	22.09	1.37	13.167 ± 0.737	1.578 ± 0.088	15.164 ± 0.849
MIPS	24	23.21	1.5	11.859 ± 0.593	1.537 ± 0.077	13.546 ± 0.677
MIPS	70	68.44	4.5	128.945 ± 12.895	16.338 ± 1.634	144.489 ± 14.449
PACS	70	68.92	2.0	174.587 ± 12.221	22.356 ± 1.565	205.312 ± 14.372
MIPS	160	152.6	9.0	391.906 ± 47.029	28.822 ± 3.459	431.668 ± 51.800
PACS	160	153.9	4.0	403.318 ± 28.232	28.642 ± 2.005	429.377 ± 30.056
SPIRE	PSW	247.1	6.0	189.055 ± 10.398	12.765 ± 0.702	197.990 ± 10.889
SPIRE	PMW	346.7	8.0	77.370 ± 4.255	5.109 ± 0.281	79.276 ± 4.360
SPIRE	PLW	496.1	12.0	26.061 ± 1.433	1.697 ± 0.093	25.907 ± 1.425

Notes. The bands not used in our modelling are indicated in boldface.

Table A.2. Summary of the images used to produce the component maps in our radiative transfer model of M 51, as well as the simulation output images used to derive the local physical parameters.

Component map		Observed images used
Old stellar disc		IRAC 3.6 μm
Young non-ionising disc	GALEX FUV, IRAC 3.6 μm , SDSS <i>r</i> , MIPS 24 μm , PACS 70 μm , PACS 160 μm	
Young ionising disc		MIPS 24 μm , IRAC 3.6 μm , H α
Dust disc	GALEX FUV, SDSS <i>r</i> , MIPS 24 μm , PACS 70 μm , PACS 160 μm	
Physical map		Model images used
SFR	GALEX FUV, MIPS 24 μm , PACS 70 μm , PACS 160 μm	
M_{star}		IRAC 3.6 μm

Notes. Indicated in bold are the image with the lowest resolution, determining the resolution of each map.